Statistical Analyses of Satellite Cloud Object Data from CERES. Part IV: Boundary-layer Cloud Objects During 1998 El Niño

Kuan-Man Xu[1], Takmeng Wong[1], Bruce A. Wielicki[1] and Lindsay Parker[2]

[1]NASA Langley Research Center, Hampton, VA
[2]Science Systems and Applications, Inc., Hampton, VA

Submitted to
Journal of Climate

Submitted, October 3, 2006

Revised, May 15, 2007; July 30, 2007

Corresponding author address:
Dr. Kuan-Man Xu
Climate Science Branch
NASA Langley Research Center
Mail Stop 420
Hampton, VA 23681
e-mail: Kuan-Man.Xu@nasa.gov

Abstract

Three boundary-layer cloud object types, overcast, stratocumulus and cumulus, that occurred over the Pacific Ocean during January-August 1998, are identified from the CERES (Clouds and the Earth's Radiant Energy System) single scanner footprint data. Characteristics of each cloud-object type matched with atmospheric states are examined for large regions in the tropics and subtropics and for different size categories. Stratocumulus cloud objects dominate the entire boundary-layer cloud population in all regions and size categories. Overcast cloud objects, which have the largest average size, are more prevalent in the subtropics and near the coastal regions, while cumulus cloud objects are prevalent over the open oceans and the equatorial regions, particularly within the small size categories. Cloud objects with equivalent diameters less than 75 km are excluded in the analysis.

The differences between the tropical and subtropical statistical distributions of cloud properties are small for liquid water path (LWP), cloud optical depth, and top-of-the-atmosphere (TOA) albedo, but large for cloud-top temperature and outgoing longwave radiation (OLR), for each of the three cloud object types. The larger cloud objects have higher LWPs, cloud optical depths, TOA albedos and OLRs, but lower SSTs and cloud top heights for the stratocumulus and overcast types. Lower-tropospheric stability seems to be the primary cause for the differences in the distributions of cloud physical properties between the regions or between the size categories. Atmospheric dynamics also play a role in determining the differences in the distributions of cloud physical properties between the size categories, but not a significant role for those between the types or between the regions. The latter may be due to uncertainties in the matched vertical velocity data. When the three cloud object types are combined in small regions, lower-tropospheric stability determines the transition of boundary-layer cloud types along a Pacific transect. The proportion of each type is the most important factor for diagnosing the combined cloud properties along this transect, such as LWP, cloud optical depth and TOA albedo. Atmospheric dynamics also play complicated roles in determining the combined cloud properties along this transect.

1. Introduction

It is well known that there are remarkable regional differences in cloud regimes associated with the Hadley and Walker circulations in the tropics and subtropics. Convective cloud systems form in the ascending regions of the Hadley and Walker circulations, e.g., deep precipitating cloud systems in the intertropical convergence zone (ITCZ), while boundary-layer clouds form predominantly in the subtropical regions associated with the descending regions of the Hadley and Walker circulations. This is related to the fact that in general, the strength of subsidence not only increases from the Tropics to the locations of the subtropical anticyclones but also varies across the ocean basins due to the Walker circulation. Another important factor for the formation of stratiform boundary-layer clouds is the cold ocean water in upwelling regions, such as off the west coasts of the continents. These areas are favorable to the formation of temperature inversions. The inversion characterizes the boundary where warm and dry air produced by the subsidence overlies the boundary-layer cloud in the top portion of a generally well-mixed layer (Wood and Bretherton 2004). The strength of the inversion and the turbulent structure of the boundary layer driven by ocean surface turbulent fluxes and radiative cooling at cloud top determine the predominant type of boundary-layer clouds. Generally speaking, stratocumulus clouds tend to form over strong subsidence or cold water regions while cumulus clouds form over weak subsidence or warm water regions, suggesting that both the large-scale dynamic and thermodynamic characteristics combine to exert an influence on the formation of different boundary-layer cloud types.

The general picture of boundary-layer cloud types in relation to the Hadley and Walker circulations outlined above, however, obscures the variabilities of cloud regimes in the tropical and subtropical regions (e.g., Klein and Hartmann 1993; Norris, 1998a, b; Weare 2000). For example, little attention has been paid to boundary-layer clouds over the tropical open oceans, where subsidence induced by deep convection (with limited spatial extent) can also form temperature inversions and produce boundary-layer clouds in the vicinities of deep convective systems. These boundary-layer clouds are less persistent and less widespread than their subtropical, west-

of-the-continents stratiform counterparts, but they are nevertheless an important contributor to the radiative energy budget and tropical dynamics (e.g., Randall et al. 1984; Greenwald et al. 1995).

Observations of boundary-layer clouds include short-term field experiments (such as ship cruises) and long-term extensive measurements from surface weather stations and satellites. The former can provide detailed case studies and understanding of physical processes by examining boundary-layer structures of turbulence and clouds (Albrecht et al. 1988, 1995; Stevens et al. 2003; Bretherton et al. 2004). As discussed in Xu et al. (2005; hereafter, Part I), case studies from field experiments, although they are invaluable for obtaining a detailed understanding of physical processes, are unable to solve the cloud-radiative feedback problem, which requires measurements made over a wide range of temporal and spatial scales (Wielicki et al. 1995). Furthermore, these field experiments took place at a few geographic locations where a specific boundary-layer cloud type dominated and the variability of cloud types was usually small.

Satellite measurements of boundary-layer clouds are most often used to study the cloud-radiative feedback problem (Rossow and Schiffer 1991, 1999; Greenwald et al. 1995; Rozendaal et al. 1995; Hahn et al. 2001; Rozendaal and Rossow 2003; Rossow et al. 2005a) because of the global coverage and the high temporal resolution of these measurements. Synoptic weather reports made by surface weather stations and ships also provide long-term observations of cloud amount, cloud type and precipitation, but not cloud microphysical and radiative properties (Norris 1998b; Hahn et al. 2001). The ISCCP (International Satellite Cloud Climatology Project; Schiffer and Rossow 1983) cloud statistical data provide useful information about cloud distributions by placing clouds in categories according to both their altitude and optical depth. Each cloud category is represented in terms of the cloud optical depth (τ)-cloud top pressure (P_c) pair. The frequencies of occurrence of different cloud categories are represented by the τ-P_c diagram with multiple τ and P_c intervals (Rossow and Schiffer 1991, 1999). The low-level clouds, which have tops at pressures greater than 680 hPa, are represented by three τ intervals that were named "cumulus" (τ from 0.1 to 3.6) "stratocumulus" (τ from 3.6 to 23) and "stratus" (τ greater than

23). These τ ranges correspond well with climatological values of these cloud types, but are not consistent with the τ ranges of these cloud types inferred from instantaneous observations by ground-based observers (Hahn et al. 2001). Hahn et al. (2001) found that the distributions of τ for the individual low cloud types overlap to such an extent that it is impossible to distinguish these cloud types from each other on the basis of τ-P_c values alone. That is, the ISCCP categories do not correspond with ground-based cloud types.

In order to isolate particular cloud processes in numerical model simulations and satellite data, compositing methods must be used to define various cloud regimes that exhibit unique processes based upon synoptic-scale conditions (Lau and Crane 1995, 1997; Tselioudis et al. 2000; Tselioudis and Rossow 2006) or statistical cloud classifications (Jakob et al. 2005; Rossow et al. 2005b; Xu et al. 2005). Examples of statistical cloud classifications include the cluster analysis of the ISCCP cloud statistical data by Jakob et al. (2005) and Rossow et al. (2005b) and the cloud object analysis of cloud system types by Xu et al. (2005). The cluster analysis uses the ISCCP cloud category frequency data on spatially large grid boxes to deduce 4-5 different cloud regimes. The method is able to deduce a boundary-layer cloud regime even in convectively dominant regions (Jakob et al. 2005).

The cloud object analysis, on the other hand, identifies a cloud object as a contiguous patch of cloudy footprints that possess similar cloud physical properties. The shape and size of a cloud object are determined by the satellite footprint data and by the selection criteria for a given cloud-system type. No arbitrary grid of the Earth is used in the analysis of satellite data, as opposed to the Eulerian approach used in the monthly-averaged satellite data. Because the selection criteria used in the cloud object analysis are based upon cloud macrophysical properties, the broad boundary-layer cloud types determined from ground-based observations can be better discriminated with the cloud object analysis than the ISCCP classification. As discussed in Part I and in section 2 of the present study, cloud fraction of satellite footprints is used to distinguish boundary-layer overcast, stratocumulus and cumulus cloud types, in decreasing order of cloud fraction.

A broader application of this cloud-object approach is the integration of observational data analysis and high-resolution modeling to improve the understanding of cloud feedbacks, as discussed in Part I and Xu et al. (2007; hereafter Part II). This includes two major steps. First, satellite data are analyzed to generate large ensembles of cloud objects, which are then combined to produce statistically robust cloud-object characteristics to reach climate accuracy (Ohring et al. 2005) for different cloud-system types. Second, the atmospheric state is matched to each cloud object in space and in time in such a way to allow for stratification of observed cloud objects according to some independent measures of the atmospheric states. This is needed to derive the partial derivatives of cloud properties versus atmospheric states, or individual components of cloud feedbacks (Schlesinger 1985).

Part I of this series outlined the details of the cloud object data analysis methodology and presented some preliminary results from the analysis of the statistical properties of tropical deep convective and three types of boundary-layer cloud objects associated with the strong 1997/98 El Niño in March 1998 and the weak 2000 La Niña in March 2000, based upon the TRMM/CERES [Tropical Rainfall Measuring Mission/Clouds and the Earth's Radiant Energy System; Wielicki et al. (1996)] footprint data. Part II presented results for deep convective cloud objects for the period of January-August 1998 while Part III presented cloud-resolving model simulation results for the observed deep convective cloud objects (Luo et al. 2007). In the present study, both the frequencies of occurrence and statistical properties of the same three types of boundary-layer cloud objects matched with atmospheric thermodynamic and dynamic states will be analyzed for the period of January-August 1998.

The objectives of this study are threefold: 1) to find similarities and differences in cloud-object physical properties between the tropical and subtropical regions and between the size categories for each of the three cloud object types, 2) to examine to what degree the cloud-object properties and the frequencies of occurrence are tied to the large-scale thermodynamic and dynamic state environments, and 3) to determine to what extent cloud-object properties of a given region can be diagnosed using statistical results of the three types of cloud objects.

The rest of the paper is organized as follows. Data and methodology are briefly outlined in section 2. The frequencies of occurrence of cloud object types are presented in section 3. Statistical properties of cloud objects matched with atmospheric states are discussed in section 4. Results of combined cloud-object types from a Pacific transect are presented in sections 5. Summary and discussion are given in section 6.

2. Data and methodology

a. Footprint data for generating cloud objects

The details of the cloud object methodology and the data used in generating the cloud object data product are presented in Part I. Briefly, the basic data from which the cloud object data are produced are a level-2 CERES Single Scanner Footprint (SSF) TOA/Surface Fluxes and Clouds data product (Wielicki et al. 1996), which includes cloud optical, microphysical (e.g., liquid water path or LWP) and macrophysical (e.g., cloud top height and temperature) properties derived using multispectral data from the Visible/Infrared Scanner (VIRS), and broadband top-of-the-atmosphere reflected shortwave (SW), emitted longwave (LW) fluxes from the CERES scanner. Only the footprint data corresponding to viewing zenith angle (VZA) less than 48° and in regions between 38° S and 38° N are used due to the restricted VZA of the VIRS instrument.

The CERES broadband radiative fluxes are produced using the new generation of Angular Distribution Models (ADMs) derived from TRMM (Tropical Rainfall Measuring Mission) CERES broadband radiance observations (Loeb et al. 2003). The cloud micro- and macro-physical properties (including cloud fraction) are retrieved from the higher-resolution VIRS cloud imager measurement (2 km x 2 km) and supplemented with sounding information from a data assimilation system. These cloud imager-based data are energy-weighted averaged over the larger CERES footprints. Details of the retrieval methods are described in the CERES algorithm theoretical basis document (Minnis et al. 1997). Uncertainties in the retrieved parameters will be described in section 2c.

b. Cloud object methodology

A cloud object is defined as a contiguous patch of cloudy regions composed of individual satellite footprints that meet a set of physically-based selection criteria. A "region-growing" strategy based on imager-derived cloud properties is used to identify cloud objects within a single satellite swath (Wielicki and Welch 1986). For all CERES footprints in a TRMM satellite orbit swath, each CERES footprint that meets the selection criteria is marked as specific cloud type. These "seed points" are grown using the Wielicki-Welch algorithm. Only footprints that are adjacent and that meet the selection criteria of a single cloud type can be joined in a cloud object. By adjacent, we mean CERES footprints that are next to each other either along the scanning direction or perpendicular to it. Cloud objects are uniquely determined when they share no adjacent footprints. Any cloud object that grows to an equivalent diameter (of a circle) of greater than 75 km (43 footprints) is saved in the cloud object database (http://cloud-object.larc.nasa.gov/). We choose an average footprint area of 10 x 10 km^2 to calculate the equivalent diameter, which can cause one-sigma error in cloud object diameter of roughly 20%.

The selection criteria for boundary-layer cloud-object types, as mentioned in section 1, are composed of both cloud-top height and cloud fraction (Table 1). The cloud-top height must be less than 3 km, which is sufficiently high to include all boundary-layer clouds. The cloud fraction of the footprint must be between 99-100% to be overcast, 40-99% to be stratocumulus and 10-40% to be cumulus. After a cloud object is identified, each footprint is checked to screen out any ice cloud footprints so that only water clouds are included in the data. The threshold of 40% for separating cumulus and stratocumulus cloud objects is arbitrary, but the lower limit of 10% for cumulus cloud objects is designed to eliminate uncertainties associated with satellite imager measurements. The overcast cloud object type was called "stratus" or "solid stratus" in Part I. It may include overcast stratocumulus and stratus clouds, which are formed by distinct boundary-layer stratifications and dynamics. These two categories of clouds cannot be distinguished from one another using the cloud object data.

The selection criteria used in this study are applied to a large area of organized cloud systems to identify a cloud object, not just to an individual footprint. The area of an individual footprint is too large to distinguish the occurrence of cumulus clouds from a small isolated stratus cloud or a small isolated stratocumulus cloud since all could have the same footprint cloud fraction. Thus, these criteria cannot describe the morphological cloud types that are seen by ground observers over a small region such as the size of a satellite footprint. Compared to the classification of boundary-layer cloud types by the ISCCP (Rossow and Schiffer 1991, 1999), which used thresholds on cloud optical depth, the current selection criteria may be more appropriate for categorizing the typically-observed, organized cloud system types. However, additional information such as imager-pixel variabilities would be needed to more rigorously categorize the morphological cloud types for individual footprint sizes seen by ground-based observers (Norris 1998a). This step is not taken because the present study is not aimed at comparing satellite data with ground-based observations and further processing of sub-footprint (i.e., the VIRS cloud imager) data is an enormous task.

The last step of the cloud object analysis methodology is to match the atmospheric state data in time and in space with the cloud objects. The procedure for matching the cloud objects with atmospheric state data was given in Part II, which utilized the latitudinal and longitudinal information of the four outermost footprints of a cloud object to draw a rectangular box that was determined by the grid coordinates of the European Center for Medium-range Weather Forecasts (ECMWF) model or another data assimilation system. The grid size was 0.5625° x 0.5625° for the ECMWF operational analysis data in the tropical/subtropical region. This box contains the entire cloud object and its immediately-adjacent surrounding area.

c. Uncertainties in the measurements

As in any type of observations, there are uncertainties in the measured/retrieved parameters examined in this study. It is challenging to assign rigorous uncertainty estimates to remotely-sensed products because direct validation measurements are scarce. The uncertainty estimates to

be provided below are based either upon the understanding of the instrument's measurement capability (Loeb et al. 2006, 2007) or upon a limited amount of direct validation measurements from ground-based instruments (Dong et al. 2002; Garreaud et al. 2001). In the latter case, the uncertainties also include those of ground-based instruments and space/time matching of surface to satellite data. The uncertainty values are listed in Table 2, along with the bin intervals of the histograms used in this study.

For the top-of-the-atmosphere albedo and LW radiative fluxes, the systematic biases are less than 0.5% while the random errors are 1-2% for LW fluxes and 2-3% for albedo, respectively (Loeb et al. 2006, 2007). These are mainly contributed by calibration and angle sampling errors. Uncertainty estimates of cloud optical depth, LWP and droplet effective radius were based upon comparisons with retrievals of the same quantities from surface-based instruments at the Atmospheric Radiation Measurement site in Oklahoma (Dong et al. 2002). The VIRS daytime retrievals agreed excellently with surface and aircraft retrievals for stratocumulus clouds (Table 2), i.e., cloud optical depth: -1.5 ± 6.2; LWP: -18 ± 41 g m^{-2}; effective radius: 0.7 ± 1.8 μm. It is expected that the errors for cumulus clouds are, however, larger for these quantities. Cloud temperature is the mean radiating temperature within a few hundred meters of the top, with errors of 0.9 ± 2.1 K, compared to that determined from surface soundings [The random error is only 1 K for oceanic clouds such as those analyzed in this study; Garreaud et al. (2001)].

These various types of uncertainties are somewhat detrimental to understanding the relationships of cloud and atmospheric dynamics. This is especially true for any small set of cloud observations such as might be examined in a short field experiment. The current study attempts to partially overcome these uncertainties by focusing on relationships derived from frequency distributions of very large samples of both clouds and atmospheric state. As shown later, the ranges of cloud and radiative flux variations in the frequency distributions far exceed the instantaneous uncertainties, as well as the systematic biases. Tests in which such errors were added to the distributions in Part II concluded that the statistical results are robust despite these errors.

d. Period of data analysis

Eight months (January-August 1998) of the TRMM CERES data are analyzed in this study. These eight months correspond to the near-peak and dissipative phases of the 1997/1998 El Niño. The TRMM orbits span the regions between 38 °S and 38 °N. Because of the TRMM inclined orbit (see Fig. 10 in Wielicki et al. 1996), the same cloud objects observed to the south of 30 °S and the north of 30 °N are identified several times a day. Exclusion of these cloud objects in this analysis allows for evenly sampling of cloud systems in different latitudinal bands. This eliminates one third of the cloud object population originally identified from this data period.

In the analyses presented later, the region between 30 °S and 30 °N is further divided into two large subregions in the tropics and subtropics. As in Rossow et al. (2005b), we define the region between 15 °S and 15 °N as the tropics and that of 15 °S to 30 °S and 15 °N to 30 °N as the subtropics. This gives nearly equal surface areas for these two subregions. But this definition of the tropics may be too narrow to include the seasonal migration of the ITCZ for all longitudes.

3. Frequency of occurrence of cloud object types

a. Geographic distribution of cloud objects

The accumulated numbers of cloud objects in 5° x 5° areas over the Pacific Ocean are shown in Figs. 1 and 2 for all cloud objects with equivalent diameters greater than 150 km and 75 km, respectively. The total number of cloud objects shown in Fig. 1 is 9161, i.e., 945 for cumulus, 5201 for stratocumulus and 3015 for overcast. There are an additional 39619 cloud objects that have equivalent diameters between 75 and 150 km shown in Fig. 2. That is, the total number of cloud objects with equivalent diameters greater than 75 km is 12026 for cumulus, 26590 for stratocumulus and 10164 for overcast cloud types, respectively. The corresponding total footprint numbers are 5.305 million and 8.362 million for the cloud objects shown in Figs. 1 and 2. This indicates that the large-size cloud objects dominate the total footprint numbers.

The geographic distributions of cloud objects have distinct features among the three cloud-object types. Except for the large-size cumulus population, there are three maximum fre-

quency centers in the subtropical regions (Figs. 1b, c and 2): one in the northern hemisphere off the coast of California, two in the southern hemisphere (i.e., central Pacific and off the South America coast). The central Pacific maximum and the westward extension of the maximum center in the northern hemisphere are related to the eastward migration of the Walker circulation during the El Niño period. The overcast cloud-object population is located further eastwards than the stratocumulus and cumulus populations and the stratocumulus population is located further eastwards than the cumulus population. There are relatively few overcast cloud objects in the equatorial region, particularly for the large size population (Fig. 1c). The aforementioned features are linked to both the longitudinal change in the strength of large-scale subsidence and the geographic distribution of SST, in particular, the cold upwelling regions off the coasts.

The geographic distributions of the total footprint numbers for the three cloud object types are shown in Fig. 3, which are somewhat comparable to the climatology of the morphological cloud types reported by ground-based observers (Norris 1998b). The frequency of occurrence, not the mean cloud amount, was shown for the observations presented in Norris (1998b). The geographic distributions shown in Fig. 3 are similar to those of Fig. 2 except that there are relatively few cumulus footprints and there are relatively few stratocumulus and overcast footprints in the tropics than in the subtropics. The ratios of the stratocumulus to the overcast cloud object footprint numbers shown in Fig. 3 are close to one near the west coasts but higher elsewhere. These ratios are generally similar to those of the morphological types in the ground-based observations if one compares the sum of Figs. 9 and 10 with the sum of Figs. 7, 8 and 11 in Norris (1998b). The ground-observed cloud types of cumulus-under-stratocumulus and stratocumulus-from-spreading-cumulus are comparable to stratocumulus objects, while the ground-observed cloud types of fair-weather stratus, ordinary stratocumulus and bad-weather stratus are comparable to overcast cloud objects. But the frequency of occurrence of cumulus cloud objects is much smaller than that of the ground-based observations, probably because these ground-based observations include many small widely-spaced cumuli, which are ignored in the cloud object analysis. Further discussion will be given in section 3b.

b. Frequency of occurrence for the tropical and subtropical regions and for different size categories

In the following, the frequency of occurrence of each cloud object type is examined for large regions in the tropics and subtropics and for different size categories. The total number of each cloud object type identified over the tropical and subtropical Pacific regions, as defined in section 2d, from the CERES SSF data is listed in "All sizes" columns of Table 3. The relative frequencies of occurrence (RFO) are shown according to the range of their equivalent diameters. Four size categories are considered. They are labeled as sizes S1, S2, S3 and S4, corresponding to the equivalent diameter ranges from 75 - 100 km (S1), 100 - 150 km (S2), 150 - 300 km (S3) and greater than 300 km (S4), respectively. The staggered size intervals were chosen because of the well-known exponential decrease of cloud population with size. The total footprint numbers in a cloud object category can provide additional information on the relative importance of a specific cloud object category to the total population. This is because the total footprint number multiplied by the average footprint size (10 x 10 km^2) corresponds to the total area coverage. It is noted that both cloudy and clear areas within a footprint are included in the total area coverage of cumulus and stratocumulus types.

The RFOs among the cloud object types and the size categories exhibit the following features. First, the smallest (S1 size) cloud objects appear much more frequently than the larger cloud objects in both the subtropics and tropics for all three cloud object types. Second, the RFOs among the four size categories of any cloud object type are nearly identical (within 2.5%) between the tropical and subtropical regions except for a doubling of the S4 overcast cloud objects in the subtropics over the tropics (11.3% vs. 5.6%).

The total footprint numbers for the all-size category in the subtropics are higher by 15% for cumulus, 48% for stratocumulus and 187% for overcast cloud objects than their tropical counterparts (Table 4) while the corresponding numbers of cloud objects in the subtropics are only higher by 11%, 19% and 53% for these three types of cloud objects, respectively (Table 3). This result can be attributed to the greater influence on the total footprint numbers from the largest size

category in the subtropics, as shown in Table 5. On the other hand, cumulus cloud objects have relatively small total footprint numbers (Table 4), compared to the overcast or stratocumulus cloud object types because they have fewer large size cloud objects (Table 3) and their averaged footprint numbers are smaller than the other two types (not shown). Reasons for this result are the exclusion of small cloud objects with equivalent diameters less than 75 km and the cutoff threshold of 10% footprint cloud fraction. The latter excludes many footprints with widely-spaced small cumulus clouds.

Obviously, there are many types of cloud footprints at a given location that do not belong to each of the three cloud object types described in this study. The first type is the footprints with cloud fractions less than 10%, which may account for the majority of the surface-observed small cumulus type (Norris 1998b). Because of the small cloud fraction within a footprint, their contributions to cloud-radiative forcings can be small. The second type is the footprints associated with small cloud objects that have equivalent diameters less than 75 km. Based upon the results for the total footprint numbers shown in Table 4, they may not contribute much to the total population. This is because the overcast and stratocumulus cloud object types are usually well organized so that there are few small cloud objects with equivalent diameters less than 75 km. But such objects may contribute more greatly to the total population of shallow cumuli. The third type is the multi-layer cloud footprints whose tops are higher than 3 km. This type is relatively rarely off the coastal regions where boundary-layer clouds dominate, but it may contribute to a half of the total cloud population elsewhere (Norman Loeb; Pers. Comm., 2007).

4. Statistical properties of cloud objects and their matched atmospheric states

a. Tropical versus subtropical regions

As in Parts I and II of this series, summary histograms of cloud physical properties are examined to illustrate the statistical similarities and differences between the tropical and subtropical boundary-layer cloud objects in this section. The summary histograms shown in Figs. 4 and 5 include all cloud objects with equivalent diameters between 75 and 300 km using between 0.5 and

1.7 million footprints for all three cloud object types in the tropical and subtropical regions. First of all, there are significant differences in all statistical distributions of cloud properties among the three cloud object types, for example, in the modes of cloud property distributions (Fig. 4) and the forms of distributions (Fig. 5). For example, the LWP distribution is exponential for cumulus, but lognormal with different modes for stratocumulus and overcast types, respectively. Similar statistical differences among the cloud-object types were identified in Part I but that analysis covered a smaller geographic region with only a month of data. They are consistent with past (Wielicki and Parker 1992; Barker et al. 1996; Barker and Wielicki 1997) and recent analyses (Szczodrak et al., 2001; Wood and Hartmann 2006). So, these differences in statistical cloud properties among the types will not be discussed in detail. Please refer to Part I for further discussion.

Second, there are significant differences in those properties that are directly related to cloud macrophysics (hereafter, cloud macrophysical properties) such as cloud top temperature (Figs. 4d-f), OLR (Figs. 4g-i) and cloud top height (not shown) between the tropical and subtropical regions. The subtropical SST distributions are much broader, with SSTs as low as 290 K, compared to a minimum SST of 295 K for the tropical distributions, although the maximum ranges are similar, at 304 K. The modes of the SST distributions (296.8 - 299.8 K) depend upon cloud-object type in the subtropical region, but relatively unchanged at 301.8 K in the tropical region (Figs. 4a-c). The large SST differences between the two regions have the most impact on cloud macrophysical properties, particularly, by shifting the modes of the OLR by 2-6 W m^{-2} (Figs. 4g-i) and those of cloud-top temperature distributions by 2-4 K and slightly broadening the subtropical distributions of cloud-top temperature for all cloud object types (Figs. 4d-f). These differences are as large as those among the types discussed earlier. They are likely influenced by the differences in both the dynamic and thermodynamic environments associated with the cloud objects to be discussed shortly.

Third, there is no discernible difference in the distributions of those properties that are directly related to cloud microphysics such as LWP (Figs. 5a-c), cloud optical depth (Figs. 5d-f) and TOA albedo (Figs. 5g-i) between the tropical and the subtropical regions [Hereafter, these

properties will be called “cloud microphysical properties” although they are also related to macrophysical properties such as the cloud thickness]. In other words, the large differences in the SST distributions (Figs. 4a-c) do not influence the distributions of these cloud microphysical properties. This result was also shown in Part I for two different climatological conditions, El Niño and La Niña. The distinct forms of cloud microphysical property distributions among the types can be resulted from distinct responses of boundary-layer processes to the large-scale dynamical and thermodynamic forcings. That is, these cloud-object types form by different processes and are characterized by different radiative properties. This important result means that the changes in cloud microphysical properties of the combined cloud types can be determined solely by those in the proportion of each of the three cloud object types because these distribution forms are independent of geographic regions and climatological conditions. So, this result will be used in section 5d to diagnose cloud microphysical property distributions of the combined cloud types in small geographic regions.

The results presented in Figs. 4 and 5 raise the following questions: First, what determines the differences in the cloud macrophysical distributions between the tropical and subtropical regions and between the cloud-object types? Second, what determines the differences in the cloud microphysical distributions between the cloud-object types? In order to answer these questions, histograms of two atmospheric dynamic and thermodynamic state variables from the ECMWF operational analysis are shown in Fig. 6. Three dynamic variables, surface divergence and ω at 700 and 500 hPa, were analyzed. These variables from the ECMWF analysis were not directly constrained by observations such as the QuickSCAT surface winds (Liu 2002). They are, therefore, highly uncertain. The differences in the distributions of surface divergence and ω at 500 hPa (ω_{500}) between the tropical and subtropical regions are similar to those in ω at 700 hPa (ω_{700}) shown in Figs. 6a-c. Two thermodynamic variables, the potential temperature differences between 700 and 1000 hPa (i.e., lower tropospheric stability or LTS; Klein and Hartmann 1993) and the estimated inversion strength (EIS; Wood and Bretherton 2006), were also analyzed. The latter may give a better indication for the nonexistence of inversion and is shown in Figs. 6d-f although

these two parameters are strongly correlated with each other for each of the three cloud object types (Dr. Zachary Eitzen; Pers. Comm., 2007).

There are two important results that are revealed in Figs. 6a-c. First, the histograms of ω_{700} show significant differences between the tropical and subtropical regions for each of the three cloud object types (Figs. 6a-c). The ω_{700} is somewhat normally distributed, with the mode being at 25 hPa day^{-1}. The cumulative frequency for all negative ω_{700} is slightly more than a half of that for all positive ω_{700}. It may be assumed that the negative ω_{700} is largely associated with the vertical motion of the environments outside the cloud objects while the positive ω_{700} is associated with that within the cloud objects themselves. For each of the three types, larger probability densities at large ω_{700} (> 70 hPa day^{-1}) can be seen in the subtropical distribution than in the tropical distribution, which is compensated by smaller probability densities at weak subsidence and weak ascent. This difference can be a major factor that contributes to the differences in the distributions of cloud macrophysical properties between the two regions discussed earlier. Second, the distributions of ω_{700} for the tropical region are rather similar among the cloud-object types, and the same is true for the subtropical region. This result may be due to the uncertainties in the ECMWF operational analysis. However, it cannot be ruled out that the responses of boundary-layer processes to the same dynamic forcings can be different for different cloud-object types.

The distribution forms of EIS are quasi-lognormal (Figs. 6d-f), compared to nearly Gaussian for ω_{700} (Figs. 6a-c). Other differences in the distributions between these two variables are as follows: First, for each of the cloud-object types, the cumulative frequency for all negative EISs in the tropical region is much higher than in the subtropical region. These differences in the EIS distributions are consistent with the fact that the strengths of the inversion for boundary-layer clouds are much stronger in the subtropics than in the tropics, due mainly to colder water in the subtropics. These differences may be expected to have a great influence on the RFOs of cloud object types examined in section 3. However, they do not seem to influence the distributions of

cloud microphysical properties much because cloud microphysical properties are largely similar between the tropical and subtropical regions for each of the three cloud-object types (Fig. 5). Second, there are significant differences in the EIS distributions between the cloud object types of a given region, as seen from the probability densities at the modes and the high EIS values and the cumulative frequencies for all negative EISs. Note that both the SST and large-scale dynamics (including horizontal advection) can influence the EIS and LTS. Although there is almost no difference in the distributions of ω_{700} between the types (Figs. 6a-c), the differences in the SST distributions between the types (Figs. 4a-c) can result in the differences in the EIS distributions seen in Figs. 6d-f, which mostly influence the cloud macrophysical distributions among the types.

It seems that neither the thermodynamic nor dynamic environments can explain the different forms of cloud microphysical property distributions for different types of cloud objects, due perhaps to inadequate ECMWF data. A possible explanation could be that boundary-layer processes respond to the large-scale dynamic and thermodynamic forcings differently for different types of cloud object ensembles. It should be noted that mesoscale cellular circulations may also play a role in determining cloud fraction (Wood and Hartmann 2006) and implicitly, the cloud object types as defined in this study.

b. Variation of subtropical cloud object properties with size

Part I presented statistical distributions of the S2 size category in a southeast Pacific region for two monthly periods. In this section, variations of cloud object properties with size will be discussed using data collected in a much larger region over an eight month period. The size dependency of cloud object properties can be used for evaluating model performance (Luo et al. 2007). For simplicity, only subtropical cloud objects will be examined because the total footprint number for each size category of cloud objects is larger in the subtropical than in the tropical regions (Table 4). For stratocumulus and overcast cloud objects, S2, S3 and S4 size categories are compared. S1, S2 and S3 size categories are compared for cumulus cloud objects because there are few cloud objects in the S4 size category (Table 3).

Because differences among size categories are small for some histograms, it is necessary to perform statistical significance tests based on the bootstrap method. The detailed procedure for this test was presented in Xu (2006). Table 6 shows the statistical significance level (p) or p-values resulting from tests between pairs of size categories of a cloud object type. The threshold p-value is customarily chosen to be 0.05. That is, there is 95% confidence that the two pdfs are significantly different. When the p-value is less than 0.05, there is more than 95% confidence that the two summary histograms are not formed from a statistically similar (cloud-object) population. It should be cautioned that there are, as discussed in section 2c, uncertainties in remotely sensed cloud parameters, especially those of cumulus clouds, so that some apparently significant differences may be in fact insignificant. Therefore, a smaller threshold p-value such as 0.01 is recommended and used in the following discussions.

For the cumulus cloud objects, the differences in the summary histograms among the three size categories (Figs. 7a, d, and g; Figs. 8a, d, and g) are small for all parameters except for albedo and cloud top height (Table 6). For the stratocumulus and overcast cloud objects, the distributions of nearly all cloud physical properties are different among the three size categories (Figs. 7b, c, e, f, h, and i; Figs. 8b, c, e, f, h, and i; Table 6). The larger cloud objects have higher LWP, higher cloud optical depths, and higher TOA albedos (Figs. 8b, c, e, f, h and i), similar to the variations of these properties of tropical deep convective cloud objects with size discussed in Part II and simulated by a cloud-resolving model in Part III. However, the larger stratocumulus/overcast cloud objects have lower SSTs, higher OLRs (Figs. 7b, c, e and f) and lower cloud-top heights (not shown), opposite to the variations of these properties of tropical deep convective cloud objects with size. As explained below, these variations of cloud macrophysical properties with size are influenced by the SST distributions and the stability of the lower troposphere while those of cloud microphysical properties may be related to the differences in large-scale dynamic environments between the size categories.

The atmospheric dynamic and thermodynamic state variables matched with the three size categories of overcast cloud objects are shown in Fig. 9. Similar diagrams for cumulus and stra-

tocumulus types are not shown because those of stratocumulus cloud objects are rather similar to those shown in Fig. 9 and there is almost no difference between the size categories for cumulus cloud objects. Fig. 9 shows that higher probability densities at the weak-to-medium surface divergence and the medium-to-strong subsidence at 700 hPa (positive ω_{700}) appear in the S4 size category than in the S2 and S3 size categories. This is not apparent in the ω_{500} distributions presumably because the surface and 700 hPa dynamic variables have stronger influences on boundary-layer clouds. The strong dynamic forcings can increase the stratus portion of the overcast cloud-object population but decrease the overcast stratocumulus portion, due to the large increase of the LTS of the S4 size category (Figs. 9d, e). The two portions of overcast objects were discussed in section 3b. The former has smaller droplet radius than the latter (see section 5 for this result), which causes the increases of the cloud optical depth and thus the TOA albedo. The OLR, on the other hand, slightly increases with size due to a decrease of cloud-top height (not shown) and possibly a large decrease of the amount of water vapor loading above the cloud top.

In summary, there are significant dependencies of nearly all cloud object properties on the horizontal size of stratocumulus and overcast types. The larger cloud objects have higher LWP, higher cloud optical depth, higher TOA albedo and higher OLR but lower SST. These results can be explained by the variations of large-scale dynamic and thermodynamic environments with cloud object size, particularly, ω_{700}, surface divergence, LTS and EIS. The differences in cumulus cloud objects between the size categories are less pronounced, due to weaker inversions associated with cumulus cloud objects and due perhaps to larger uncertainties in remotely-sensed measurements of broken clouds than those of contiguous clouds.

5. Transition of cloud object types along a Pacific transect

Sections 3 and 4 have examined the RFOs and statistical properties of boundary-layer cloud object types in large regions of the tropical and subtropical Pacific Ocean, respectively. However, statistical cloud properties and RFOs can vary greatly from one small region to another. In this section, a transect is chosen to further examine the variability of these cloud object charac-

teristics. The transect is defined by a GCSS (GEWEX Cloud System Study, where GEWEX stands for Global Energy and Water-cycle Experiment) model intercomparison project (Siebesma et al. 2004) and encompasses an area from the California coast [centered at (125 °W, 35 °N)] to the equator [centered at (173 °W, 1 °S); Fig. 10]. This transect is used by GCSS to examine the transition from subtropical boundary-layer clouds to tropical deep convection. Each of the seven regions (labeled Grids 1-7) along this transect is 6 °x 6 ° in size.

a. Climatology of the atmospheric dynamic and thermodynamic states

The ECMWF data at 6-hourly interval over the eight month period are used to calculate the means and standard deviations of atmospheric dynamic and thermodynamic state variables over each of the seven 6 °x 6 ° grids. The means of the dynamic state variables, ω_{700}, ω_{500} and surface divergence, do not change much along the GCSS transect (Fig. 11), compared to the temporal variabilities as measured by the standard deviations. The standard deviations of these variables are large, especially in the surface divergence at all grids. It is noted that the means of ω_{700} vary from -14 hPa day^{-1} at Grid 7 (at the equator) to 42 hPa day^{-1} at Grid 2, covering a significant portion of the dynamic state ranges defined by Bony et al. (2004). On the other hand, the thermodynamic state variables, the LTS and EIS, have significant differences among the seven grids in both the means and standard deviations. The means of the LTS and EIS are generally higher in the higher-latitude grids than in the lower-latitude grids, and so are the standard deviations. The latter is due primarily to the larger seasonal variations of SSTs in the higher latitudes than in the lower latitudes. The pronounced trends of LTS and EIS along the GCSS transect are the major reason for the transition of different cloud-object types to be presented below.

b. Relative frequency of occurrence of cloud object types

As in section 3b, the proportion of total accumulated footprint numbers along the transect will be examined for each of the three cloud object types in detail. The total accumulated footprint numbers and the total cloud object numbers are also listed in Table 7. Both the total cloud object

number and the total accumulated footprint number generally decrease from the California coast to the equator along the GCSS transect. This is related to the climatology of the thermodynamic stability discussed above. There are, however, two minor exceptions. One is that Grid 3 has a few more cloud objects than Grid 2. The other is that Grid 2 has the highest total accumulated footprint number and thus the averaged size of cloud objects is the largest at Grid 2.

As in the results shown in section 3b, stratocumulus cloud objects dominate the total boundary-layer cloud-object population at all grids except for Grids 1 and 2 where the overcast cloud objects dominate (Table 7). This is expected because these two grids are located near the California coast with large stabilities. Along this transect, the overcast clouds are more prevalent near the coastal regions while cumulus clouds are more prevalent over the open oceans (e.g., Grid 7). Grid 2 has the lowest cumulus population while its stratocumulus population is also relatively low. Thus, the presence of the large proportion of overcast cloud objects at this grid dominates the overall characteristics of cloud physical property distributions to be shown below.

c. Properties of the combined cloud object types

The transition from overcast-dominated to cumulus-dominated regions across the GCSS transect is best represented by changes in cloud microphysical properties (i.e., LWP, cloud optical depth and TOA albedo; Figs. 12a-c). At Grids 1 and 2, histograms of these parameters resemble those characterized by the overcast cloud type discussed in section 4 more than the other grids. Also, the probability densities are higher in the high ranges of TOA albedo, LWP and τ, which are typically observed only for the overcast cloud objects (Figs. 5c, f, i). At the lower-latitude grids (e.g., Grids 5-7), histograms of these parameters resemble lognormal distributions with narrow peaks, typical of cumulus and stratocumulus types shown in Figs. 5a, b, d, e, g, h. The peak probability densities at the modes increase as the grid moves further away from the coast. This indicates the transition from stratocumulus to cumulus types although purely exponential distributions for LWP and τ, typical of cumulus cloud objects (Figs. 5a and d), are not observed at either Grid 6 or 7. On the other hand, the contribution to the histograms by stratocumulus cloud objects

at Grid 1 is obvious, as evidenced by a two-mode distribution in TOA albedo and significant probability densities at low LWP and τ (Figs. 12a-c) and compared to those distributions at Grid 2. The droplet radius histograms can be divided into two groups, small droplet radii for the stratus-dominated regions for Grids 1 and 2 and larger droplet radii for other five grids (Fig. 13e). Note that the retrieved droplet radii are representative of those near cloud tops. These two droplet size features are due to the influence of continental aerosols and the transition of cloud-object types along the transect.

The overcast-to-cumulus transition across this Pacific transect is not dramatic in cloud macrophysical properties. But there are a few interesting features that worth pointing out. First, the gradual shifts in the modes of the distributions in cloud-top temperature (not shown), OLR (Fig. 13b) and cloud-top heights (Fig. 13d) are readily seen, except for Grid 1. They are associated with the shifts in the SST distributions (Fig. 13a). Second, the SST distributions are relatively flat for Grids 1 and 2, which are associated with large seasonal variations of SST near the California coast. Third, the shifts in the modes of OLR and cloud-top height generally follow those of SST. This is also partially due to the transition of cloud-object types since optically thin clouds are associated with higher OLR. Lastly, the cloud-top height distribution is more complicated. This is partly due to the use of a fixed lapse rate to diagnose the height from the difference between SST and cloud-top temperature (Garreaud et al 2001). As seen from Fig. 11, the LTS varies greatly along the transect.

The relationships between the atmospheric dynamic and thermodynamic state variables and cloud properties along this transect (Figs. 13c and f) are more complicated than those presented in section 4. These relationships cannot be deduced from the climatology of the dynamic and thermodynamic variables discussed earlier (Fig. 11). First, subsidence is the strongest at the equator (i.e., Grid 7) and there is almost no negative ω_{700}. This can be attributed to the highest SST there (Figs. 13a), which is not favorable to the formation of boundary-layer clouds. Therefore, large subsidence is thus needed to form these clouds in the vicinity of deep convection. However, Grid 6 has less subsidence than in Grid 5, suggesting that horizontal advection may

play a more significant role in Grid 6 than in Grid 5. Second, the stability as measured by the EIS is large at the three grids closest to the coast, in particular, at Grid 1 (EIS > 5 K). The EIS is less than 3 K at the other four grids. But there are significant probability densities at the negative ω_{700} ranges only at Grids 1 and 2 (not Grid 3). This result implies that the stability in the boundary layer of these regions is not controlled by the strength of the subsidence, but possibly influenced by horizontal advection. Third, the transition of cloud object types along the transect depends upon the thermodynamic environment, rather than the dynamic environment. This result is independent of which dynamic variable is used. For example, Grid 4 has the largest subsidence at 500 hPa and there is almost no positive ω_{500} at Grid 1 (not shown).

d. Diagnosis of the properties of the combined cloud object types

In most small regions, all cloud-object types coexist due to large variabilities of the atmospheric dynamic and thermodynamic environments. Section 4 indicates that the changes in cloud microphysical properties of the combined cloud types can be determined primarily by changes in the proportions of these three cloud object types because the forms of cloud microphysical property distributions are independent of geographic regions and climatological conditions (see Part I). This hypothesis can be tested by using the observed proportions of the three cloud object types along this transect (Table 7) and the distribution forms presented in section 4. The diagnostic relationship can be expressed by

$$PDF_{all} = A_{cu}PDF_{cu} + A_{sc}PDF_{sc} + A_{oc}PDF_{oc}$$

where A_x is the proportion of each cloud object type (Table 7), and the PDF_x is the pdf of each cloud-object type presented in section 4. Subscripts *cu*, *sc*, *oc* and *all* denote cumulus, stratocumulus, overcast types and the combined cloud objects, respectively.

The diagnosed histograms are shown in Figs. 12d-e and can be directly compared to the observed ones shown in Figs. 12a-c. The agreement is good in general except that the diagnosed histograms at Grid 4 are identical to those at Grid 5 because the proportions of cloud object types are nearly identical (Table 7). This result illustrates the importance of separating the boundary-

layer clouds into distinct types, as done in sections 3-4. The RFOs for each cloud object type and each cloud object size, which are linked to local thermodynamic stability, SST distribution, and perhaps dynamics, will then determine the overall cloud property distributions in a region. A similar diagnosis was made for cloud macrophysical properties (not shown). As expected, the results do not agree with observations at all because the distribution forms of these properties are also highly dependent on local atmospheric state variables such as SST.

6. Summary and discussion

Three boundary-layer cloud object types, overcast, stratocumulus and cumulus, that occurred over the Pacific Ocean during January-August 1998, have been examined using the CERES SSF data from the TRMM satellite. This study has emphasized the contrasts and similarities in the characteristics of each cloud-object type for large regions in the tropics and the subtropics and for different size categories, in relation to the atmospheric dynamic and thermodynamic environments. Both the frequencies of occurrence and statistical distributions of cloud physical properties and atmospheric state variables are analyzed for each of the three cloud object types.

For the frequencies of occurrence, stratocumulus type dominates the total boundary-layer cloud-object population that has equivalent diameters of cloud objects greater than 75 km in all regions and size categories. Overcast type is more prevalent in the subtropics and near the coastal regions while cumulus type is most prevalent over the open oceans and the equatorial regions, particularly within the small size categories. If cloud objects with equivalent diameters less than 75 km were included in the analysis, cumulus type might dominate the total cloud-object population but not its total footprint numbers in the tropics, which are more important than the total numbers of cloud objects for determining the cloud properties of the combined cloud object types. The large-size overcast cloud objects with equivalent diameters greater than 300 km occur more frequently in the subtropics than in the tropics, due to large differences in the thermodynamic environment. They have much larger average size than their cumulus and stratocumulus counterparts. The proportion of each cloud object type in smaller geographic regions is even more strongly tied

to the large-scale thermodynamic environment than in the large regions of the tropical and subtropical Pacific Ocean.

The differences between the tropical and subtropical statistical distributions of cloud properties from large ensembles of cloud objects are small for liquid water path, cloud optical depth, and TOA albedo, but large for cloud-top temperature and OLR, for each of the three types. The differences in cloud-top temperature and OLR are strongly linked to the differences in the atmospheric dynamic and thermodynamic environments between the tropical and subtropical regions. However, the differences in the atmospheric dynamic environments are negligible and those in the thermodynamic environments are relatively small between the types despite the fact that the statistical distributions of all cloud microphysical and macrophysical properties are significantly different between the types (see also Part I). This result may be due to the inability of the ECMWF model to properly assimilate the differences in atmospheric states between the cloud object types.

There are significant dependencies of nearly all cloud object properties on the horizontal size of stratocumulus and overcast types. The larger cloud objects have higher LWP, higher cloud optical depth, higher TOA albedo and higher OLR but lower SST. These results can be explained by the variations of large-scale dynamic and thermodynamic environments with cloud object size, particularly the subsidence at 700 hPa, surface divergence and the estimated inversion strength, despite of large uncertainties in the ECMWF analysis of these variables. However, preliminary comparisons of the surface divergences between ECMWF and QuikSCAT observations (Liu 2002) show large differences for cloud objects identified from the Terra satellite. Therefore, this current result should be viewed with caution. The differences in cumulus cloud objects between the size categories are less pronounced, due to weaker inversions associated with cumulus cloud objects and due perhaps to larger uncertainties in remotely-sensed measurements of broken clouds than those of contiguous clouds.

When the three cloud object types are combined in small regions, the lower-tropospheric stability determines the transition of boundary-layer cloud types along a Pacific transect. The proportion of each type is the most important factor for diagnosing the combined cloud microphysi-

cal properties along this transect, such as LWP, cloud optical depth and TOA albedo. This illustrates the importance of separating the boundary-layer clouds into distinct types, as discussed in Part I and this study, because cloud microphysical property distributions of each type are independent of the large-scale environments. The atmospheric dynamics also play complicated roles in determining the combined cloud macrophysical properties along this transect.

Part I found that the proportion of different boundary-layer cloud-object types is changed as the large-scale circulations are changed from El Niño to La Niña conditions but some statistical cloud properties do not change for a size category of cloud objects with equivalent diameters between 100 and 150 km. This study has, however, found that there are some dependencies of LWP, cloud optical depth, TOA albedo, cloud-top height and OLR and SST on cloud object size, particularly for the stratocumulus and overcast types. This suggests that the proportion of different size categories of a cloud object type is also an important factor in accurately determining the overall cloud properties in a region. This proportion seems to change from one region to another due primarily to differences in the thermodynamic environments. Implication of this result is that the changes in the frequency of occurrences between the size categories are also important in determining the changes in the overall cloud properties and cloud-radiative forcings.

Bony and Dufresne (2005) suggested that a better understanding of the behavior of boundary-layer clouds with changing environmental conditions will be critical to reduce the uncertainty in model predictions of tropical cloud feedbacks and climate sensitivity. This will require an even larger volume of cloud objects than presented in this study, in order to increase the robustness of the estimated change in cloud properties with respect to atmospheric states. The rigorous statistics from large ensembles of cloud objects will produce the climate accuracy necessary for estimating the individual components of cloud feedbacks.

These current results are based upon eight months of the TRMM CERES data. It will be interesting to investigate these cloud object types using the Terra and Aqua CERES data, especially their relationships with the atmospheric states. The cloud macrophysical properties of the Terra and Aqua CERES data are retrieved from higher-resolution imagers with smaller uncertain-

ties than those of TRMM CERES data. The atmospheric states such as the surface divergence may be more reliable due to the assimilation of QuikSCAT surface wind data (Liu 2002) into meteorological model analyses for the recent data period. The effort of producing a large volume of cloud object data from the Terra and Aqua CERES data is currently underway and the new results will be reported in a future study.

Acknowledgments: The CERES data were obtained from the Atmospheric Sciences Data Center at the NASA Langley Research Center. This research has been supported by NASA EOS interdisciplinary study and Modeling, Analysis and Prediction programs (Dr. Donald Anderson, Program Manager) and by the NSF grant ATM-0336762. The authors would also like to acknowledge Dr. Bruce Barkstrom of NOAA National Climatic Data Center and Professor David Randall of Colorado State University for their earlier insightful vision to this project. Dr. Zachary Eitzen is thanked for subsetting the atmospheric state variables used in this study. We thank two anonymous reviewers for their constructive comments.

References

Albrecht, B. A., D. A. Randall, and S. Nicholls, 1988: Observations of marine stratocumulus clouds during FIRE. *Bull. Amer. Meteor. Soc.*, **69,** 618-626.

Albrecht, B. A., C. S. Bretherton, D. Johnson, W. H. Schubert, and A. S. Frisch, 1995: The Atlantic Stratocumulus Transition Experiment -- ASTEX. *Bull. Amer. Meteor. Soc.,* **76,** 889-904.

Barker, H. W. and B. A. Wielicki, 1997: Parameterizing grid-averaged longwave fluxes for inhomogeneous marine boundary layer clouds. *J. Atmos. Sci.*, **54**, 2785-2798.

Barker, H. W., B. A. Wielicki, and L. Parker, 1996: A parameterization for computing grid-averaged solar fluxes for inhomogeneous marine boundary layer clouds. Part II: Validation using satellite data. *J. Atmos. Sci.*, **53**, 2304-2316.

Bony, S., and J.-L. Dufresne, 2005: Marine boundary layer clouds at the heart of tropical cloud feedback uncertainties in climate models, *Geophys. Res. Lett.*, **32,** L20806, doi:10.1029/2005GL023851.

Bony, S., J.-L. Dufresne, H. Le Treut, J.-J. Morcrette and C. Senior, 2004: On dynamic and thermodynamic components of cloud changes. *Climate Dyn.,* **22,** 71-86. doi: 10.1007/s00382-003-0369-6.

Bretherton, C. S., and coauthors, 2004: The EPIC 2001 stratocumulus study. *Bull. Amer. Meteor. Soc.,* **85,** 967-977.

Dong, X., P. Minnis, G. G. Mace, W. L. Smith, Jr., M. Poellot, R. T. Marchand, and A. D. Rapp, 2002: Comparison of stratus cloud properties deduced from surface, GOES, and aircraft data during the March 2000 ARM cloud IOP. *J. Atmos. Sci.*, **23,** 3265-3284.

Garreaud, R. D., J. Rutllant, J. Quintana, J. Carrasco, and P. Minnis, 2001: CIMAR-5: A snapshot of the lower troposphere over the subtropical southeast Pacific. *Bull. Amer. Meteor. Soc.*, **82,** 2193-2207.

Greenwald, T. J., G. L. Stephens, S. A. Christopher, and T. H. Vonder Haar, 1995: Observations of the global characteristics and regional radiative effects of marine cloud liquid water. *J. Climate*, **8,** 2928-2946.

Hahn, C. J., W. B. Rossow, and S. G. Warren, 2001: ISCCP cloud properties associated with standard cloud types identified in individual surface observations. *J. Climate,* **14,** 11-28.

Jakob, C., G. Tselioudis, and T. Hume, 2005. The radiative, cloud and thermodynamic properties of the major Tropical Western Pacific cloud regimes. *J. Climate*, **18,** 1203-1215.

Klein, S. A., and D. L. Hartmann, 1993: The seasonal cycle of low stratiform clouds. *J. Climate,* **6,** 1587-1606.

Lau, N.-C., and M. W. Crane, 1995: A satellite view of the synoptic-scale organization of cloud properties in midlatitude and tropical circulation systems. *Mon. Wea. Rev.,* **123,** 1984-2006.

Lau, N.-C., and M. W. Crane, 1997: Comparing satellite and surface observations of cloud patterns in synoptic-scale circulation systems. *Mon. Wea. Rev.,* **125,** 3172-3189.

Loeb, N. G., N. Manalo-Smith, S. Kato, W. F. Miller, S. K. Gupta, P. Minnis, and B. A. Wielicki, 2003: Angular distribution models for top-of-atmosphere radiative flux estimation from the Clouds and the Earth's Radiant Energy System instrument on the Tropical Rainfall Measuring Mission satellite. Part I: Methodology. *J. Appl. Meteor.,* **42,** 240–265.

Loeb, N. G., S. Kato, K. Loukachine, N. Manalo-Smith, and D. R. Doelling, 2007: Angular distribution models for top-of-atmosphere radiative flux estimation from the Clouds and the Earth's Radiant Energy System Instrument on the Terra satellite. Part II: Validation. *J. Atmos. Oceanic Tech.,* **24,** 564–584.

Loeb, N. G., W. Sun, W. F. Miller, K. Loukachine, and R. Davies, 2006: Fusion of CERES, MISR, and MODIS measurements for top-of-atmosphere radiative flux validation. *J. Geophys. Res*., **111**, D18209, doi:10.1029/2006JD007146.

Liu, W. T., 2002: Progress in scatterometer application. *J. Oceanogr.,* **58,** 121-136.

Luo, Y., K.-M. Xu, B. A. Wielicki, T. Wong and Z. A. Eitzen, 2007: Statistical analyses of satellite cloud object data from CERES. Part III: Comparison with cloud-resolving model simulations of tropical convective clouds. *J. Atmos. Sci.,* **64,** 762–785.

Minnis, P.; D. Y. Young, D. P. Kratz; J. A. Coakley, Jr.; M. D. King, D. P. Garber, P. W. Heck, S. Mayor, and R. F. Arduini, 1997: Cloud Optical Property Retrieval (Subsystem 4.3). "Clouds and the Earth's Radiant Energy System (CERES) Algorithm Theoretical Basis Document, Volume III: Cloud Analyses and Radiance Inversions (Subsystem 4)," edited by CERES Science Team, December, 1997, 60 pp. [http://asd-www.larc.nasa.gov/ATBD/ATBD.html]

Norris, J. R., 1998a: Low cloud type over the ocean from surface observations. Part I: Relationship to surface meteorology and the vertical distribution of temperature and moisture. *J. Climate,* **11,** 369-382.

Norris, J. R., 1998b: Low cloud type over the ocean from surface observations. Part II: Geographic and seasonal variations. *J. Climate,* **11,** 383-403.

Ohring, G., B. A. Wielicki, R. Spencer, B. Emery and R. Datla, 2005: Satellite instrument calibration for measuring global climate change. Report of a workshop. *Bull. Amer. Meteor. Soc.,* **86,** 1303-1313, doi: 10.1175/BAMS-86-9-1303.

Randall, D. A., J. A. Coakley Jr., C. W. Fairall, R. A. Kropfli, and D. H. Lenschow, 1984: Outlook for research on subtropical marine stratiform clouds. *Bull. Amer. Meteor. Soc.,* **65,** 37-40.

Rossow, W. B., and R. A. Schiffer, 1991: ISCCP cloud data products. *Bull. Amer. Meteor. Soc.,* **72**, 2-20.

Rossow, W. B., and R. A. Schiffer, 1999: Advances in understanding clouds from ISCCP. *Bull. Amer. Meteor. Soc.*, **80**, 2261-2287.

Rossow, W. B., Y. Zhang, and J. Wang, 2005a: A statistical model of cloud vertical structure based on reconciling cloud layer amounts inferred from satellites and radiosonde humidity profiles. *J. Climate,* **18,** 3587-3605.

Rossow, W. B., G. Tselioudis, A. Polak, and C. Jakob, 2005b: Tropical climate described as a distribution of weather states indicated by distinct mesoscale cloud property mixtures. *Geophys. Res. Lett.*, **32,** L21821, doi:10.1029/2005GL024584.

Rozendaal, M. A., and W. B. Rossow, 2003: Characterizing some of the influences of the general circulation on subtropical marine boundary-layer clouds. *J. Atmos. Sci.,* **60,** 711-728.

Rozendaal, M. A., C. B. Leovy, and S. A. Klein, 1995: An observational study of diurnal variations of marine stratiform cloud. *J. Climate,* **8,** 1795-1809.

Schiffer, R. A., and W. B. Rossow, 1983: The International Satellite Cloud Climatology Project (ISCCP): The first project of the World Climate Research Programme. *Bull. Amer. Meteor. Soc.,* **64,** 779-784.

Schlesinger, M. E., 1985: Feedback analysis of results from energy balance and radiative-convective models. Projecting the Climatic Effects of Increasing Carbon Dioxide, M. C. MacCracken and F. M. Luther, Eds., U.S. Department of Energy, 280–319.

Siebesma, A. P., and coauthors, 2004: Cloud representation in general-circulation models over the northern Pacific Ocean: A EUROCS intercomparison study. *Quart. J. Roy. Meteor. Soc.,* **130,** 3245-3268.

Stevens, B., and coauthors, 2003: Dynamics and Chemistry of Marine Stratocumulus -- DYCOMS-II, 2003: *Bull. Amer. Meteor. Soc.*, **84,** 579-593.

Szczodrak, M., P. H. Austin, and P. B. Krummel, 2001: Variability of optical depth and effective radius in marine stratocumulus clouds. *J. Atmos. Sci.,* **58,** 2912-2926.

Tselioudis, G., and W. B. Rossow, 2006: Climate feedback implied by observed radiation and precipitation changes with midlatitude storm strength and frequency. *Geophy. Res. Lett.,* **33,** L02704, doi:10.1029/2005GL024513.

Tselioudis, G., Y. Zhang, and W. B. Rossow, 2000: Cloud and radiation variations associated with northern midlatitude low and high sea level pressure regimes. *J. Climate,* **13,** 312-327.

Weare, B. C., 2000: Near-global observations of low clouds. *J. Climate,* **13,** 1255-1268.

Wielicki, B. A., and Parker, L. 1992: On the determination of cloud cover from satellite sensors: The effect of sensor spatial resolution. *J. Geophys. Res.*, **97**, 12,799-12,823.

Wielicki, B. A., and R. M. Welch, 1986: Cumulus cloud properties derived using Landsat satellite data. *J. Clim. Appl. Meteor.,* **25,** 261-276.

Wielicki, B. A., R. D. Cess, M. D. King, D. A. Randall, and E. F. Harrison, 1995: Mission to Planet Earth: Role of clouds and radiation in climate. *Bull. Amer. Meteor. Soc.,* **76,** 2125-2153.

Wielicki, B. A., B. R. Barkstrom, E. F. Harrison, R. B. Lee III, G. L. Smith, and J. E. Cooper, 1996: Clouds and the Earth's Radiant Energy System (CERES): An Earth Observing System Experiment. *Bull. Amer. Meteor. Soc.*, 77, 853-868.

Wood, R., and C. S. Bretherton, 2004: Boundary layer depth, entrainment, and decoupling in the cloud-capped subtropical and tropical marine boundary layer. *J. Climate,* **17,** 3576–3588.

Wood, R. and C. S. Bretherton, 2006: On the relationship between stratiform low cloud cover and lower-tropospheric stability. *J. Climate,* **19,** 6425–6432.

Wood, R., and D. L. Hartmann, 2006: Spatial variability of liquid water path in marine low cloud: The importance of mesoscale cellular convection. *J. Climate,* **19,** 1748-1764.

Xu, K.-M., 2006: Using the bootstrap method for a statistical significance test of differences between histograms. *Mon. Wea. Rev.*, **134,** 1442-1453.

Xu, K.-M., T. Wong, B. A. Wielicki, L. Parker, and Z. A. Eitzen, 2005: Statistical analyses of satellite cloud object data from CERES. Part I: Methodology and preliminary results of 1998 El Niño/2000 La Niña. *J. Climate,* **18,** 2497-2514.

Xu, K.-M., T. Wong, B. A. Wielicki, L. Parker, B. Lin, Z. A. Eitzen, and M. Branson, 2007: Statistical analyses of satellite cloud object data from CERES. Part II: Tropical convective cloud objects during 1998 El Niño and evidence for supporting the fixed anvil temperature hypothesis. *J. Climate,* **20,** 819-842.

List of figures

stratocumulus and overcast size categories have equivalent diameters of 100-150 km, 150-300 km and greater than 300 km, respectively.

Figure 8. Same as Fig. 5 except for three size categories of subtropical cumulus (a, d and g), stratocumulus (b, e and h) and overcast (c, f and i) cloud objects. The cumulus size categories have equivalent diameters of 75-100 km, 100-150 km and 150-300 km, respectively. The stratocumulus and overcast size categories have equivalent diameters of 100-150 km, 150-300 km and greater than 300 km, respectively.

Figure 9. Histograms of cloud-object matched ω vertical velocity at 500 hPa (a) and 700 hPa (b), surface divergence (c), lower-tropospheric stability (d) and estimated inversion strength (EIS; e) for three size categories of the overcast cloud object type in the subtropical region. The lower-tropospheric stability is defined as the potential temperature difference between 700 and 1000 hPa by Klein and Hartmann (1993). The EIS is defined in Wood and Bretherton (2006).

Figure 10. Locations of grids along a Pacific cross section (Grid 1-7) designed by the GCSS for a model intercompairson project. The accumulated number of all three cloud object types in 5° x 5° grids with equivalent diameters greater than 75 km is also shown.

Figure 11. Eight-month (January - August 1998) means (lines within the bars) and standard deviations (vertical bars) of selected atmospheric-state parameters for Grids 1-7 of the GCSS Pacific transect: from the top to bottom panels, ω_{500}, ω_{700}, surface divergence, lower tropospheric stability [LTS; θ(700 hPa) - θ (1000 hPa)], and estimated inversion strength (EIS), respectively.

Figure 12. Summary histograms of liquid water path (a, d), cloud optical depth (b, e) and top-of-the-atmosphere albedo (c, f) for the combined cloud object types along the seven grids of the GCSS Pacific transect. Grid numbers along the transect are indicated by different colors. See Fig. 10 for the location of these grids. The left panels (a-c) are from observations

while the right panels (d-f) are diagnosed from the observed proportions of cloud object types and histograms shown in Fig. 5.

Figure 13. Same as Figs. 12a-c except for SST (a), OLR (b), ω_{700} (c), cloud-top height (d), droplet radius (e) and estimated inversion strength (f). A five-point (with weighting factors of 1/17, 3/17, 9/17, 3/17, 1/17) smoothing was applied to the histogram before plotting.

List of tables

Table 1. A list of selection criteria for the boundary-layer cloud types.

Table 2. The systematic biases and random errors in the measured footprint data of boundary-layer clouds and bin intervals of histogram used in this study.

Table 3. Percent of the number of cloud-objects in the tropical and subtropical Pacific for four size categories of boundary-layer cumulus, stratocumulus and overcast cloud-object types during January-August 1998. The equivalent diameters of S1, S2, S3 and S4 size categories range from 75-100 km, 100-150 km, 150-300 km and > 300 km, respectively. The numbers of all-size (S1, S2, S3 and S4 combined) cloud objects of a given type are also shown in the table.

Table 4. Same as Table 3 except for the total footprint numbers, which are proportional to the total area coverages, for each size category in the tropical and subtropical regions. The total footprint numbers for all sizes are in thousands.

Table 5. Statistics of the footprint numbers for the S4 size (equivalent diameters greater than 300 km) categories of boundary-layer cloud object types in the tropical and subtropical regions.

Table 6. The statistical significance levels or *p* values between a pair of size categories for different parameters of the three subtropical boundary-layer cloud object types. See text for the definition of size categories S1, S2, S3 and S4 and an explanation of *p* values.

Table 7. Percent of total footprint number of each cloud object type observed in each 6° x 6° grid along the GCSS transect during January-August 1998. The total footprint number and cloud object number of all types are shown. See Fig. 10 for the location of each grid box.

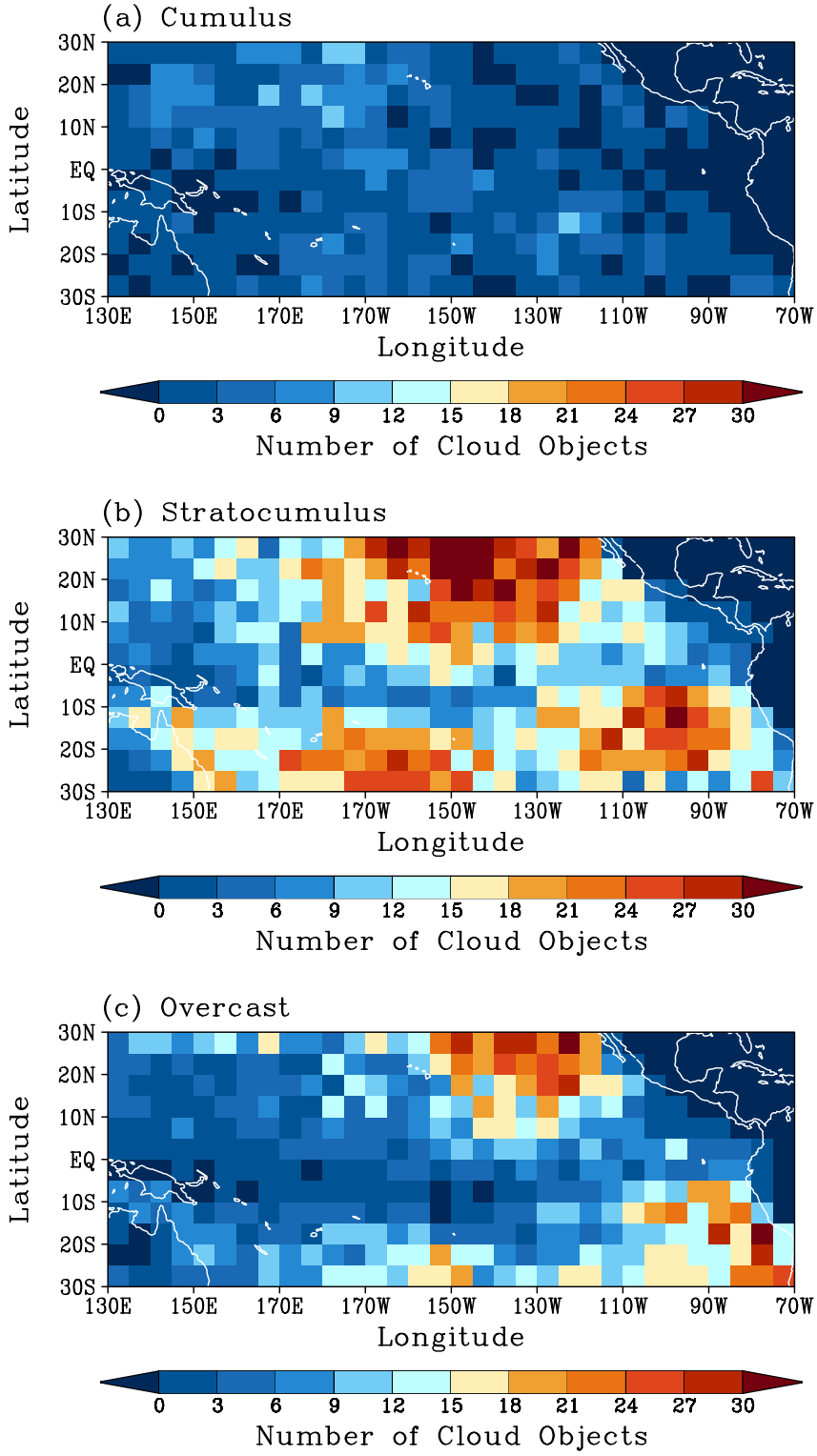

Figure 1. The accumulated number of cloud objects in 5° x 5° grids with equivalent diameters greater than 150 km observed during January - August 1998. The top panel is for the cumulus cloud objects, the middle the stratocumulus cloud objects and the bottom the overcast cloud objects.

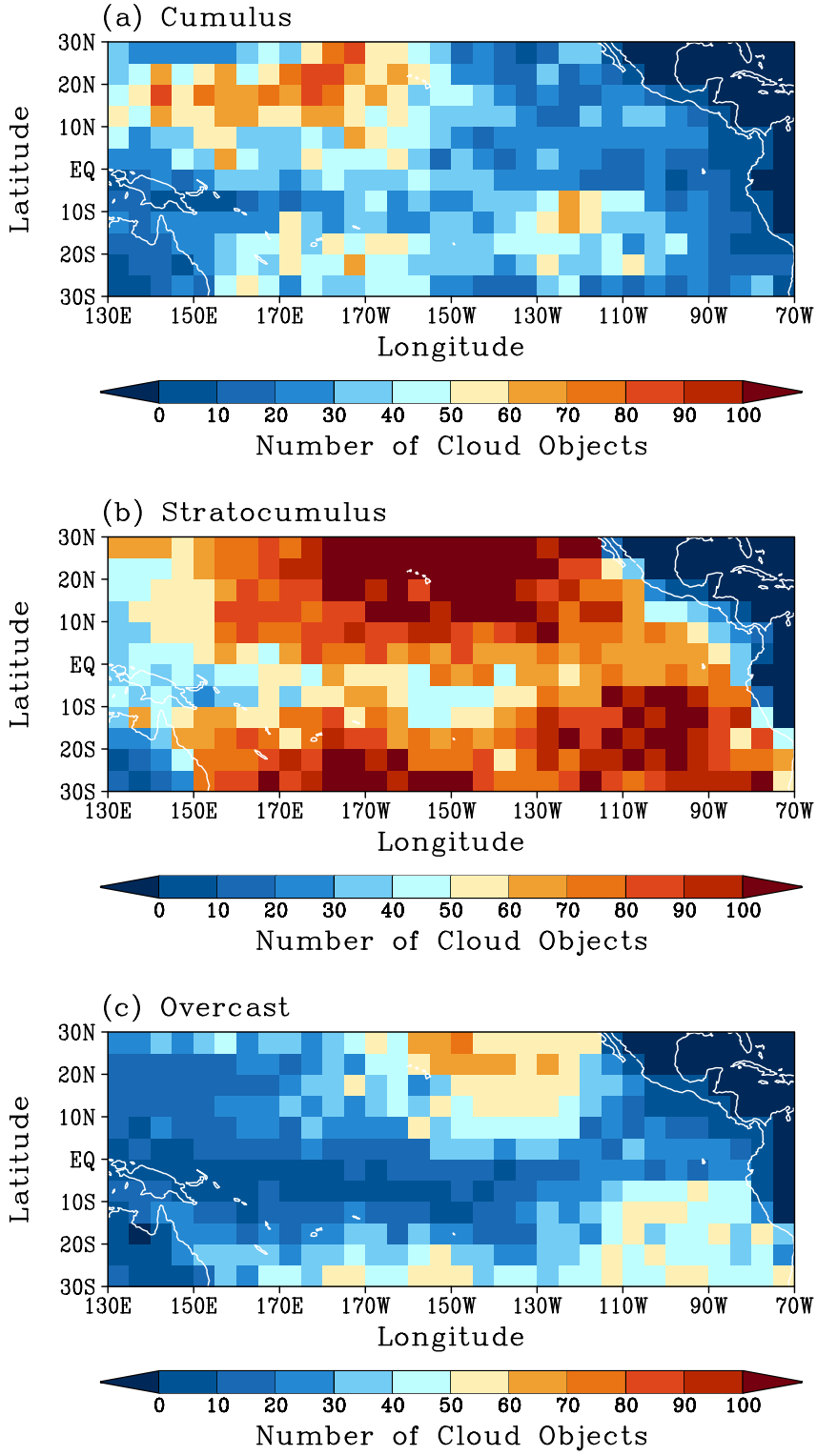

Figure 2. Same as Fig. 1 except for cloud objects with equivalent diameters greater than 75 km (including those large cloud objects shown in Fig. 1).

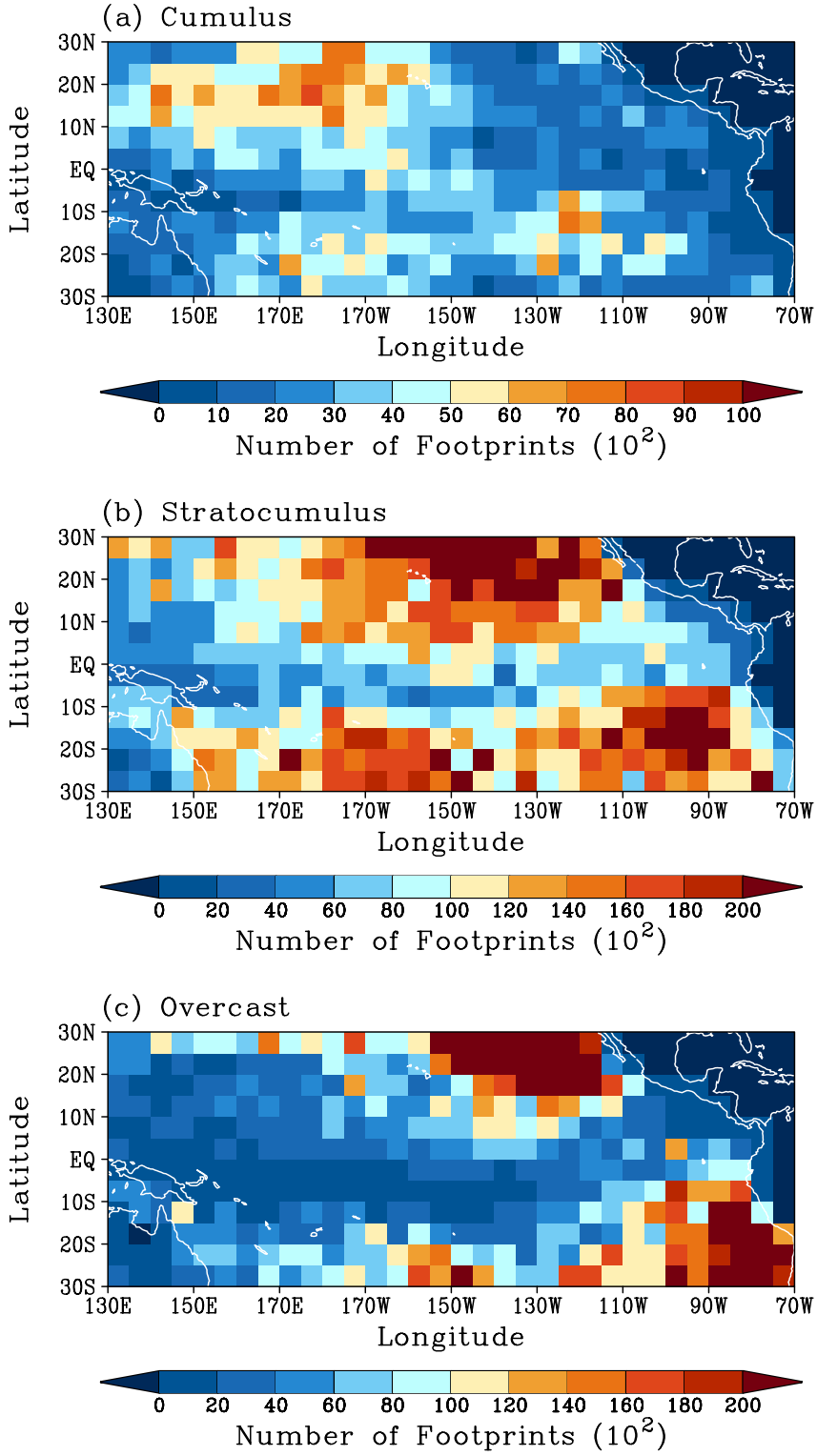

Figure 3. Same as Fig. 2 except for the total footprint numbers in 5° x 5° grids.

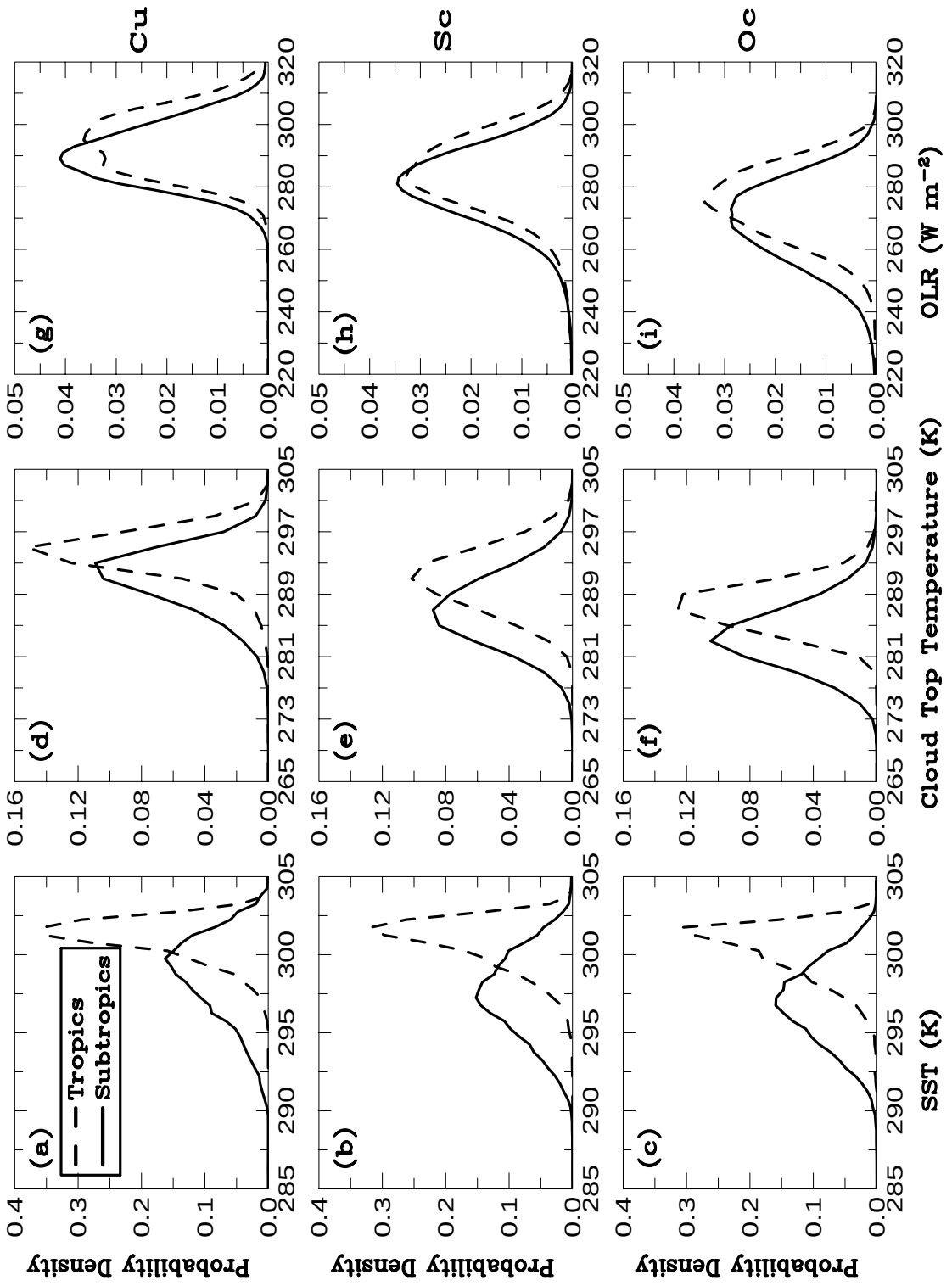

Figure 4. Summary histograms of sea surface temperature (a-c), cloud-top temperature (d-f) and outgoing longwave radiation flux (g-i) for boundary-layer cumulus (a, d and g), stratocumulus (b, e and h) and overcast (c, f and i) cloud objects with equivalent diameters between 75 and 300 km in the tropical and subtropical regions for January - August 1998.

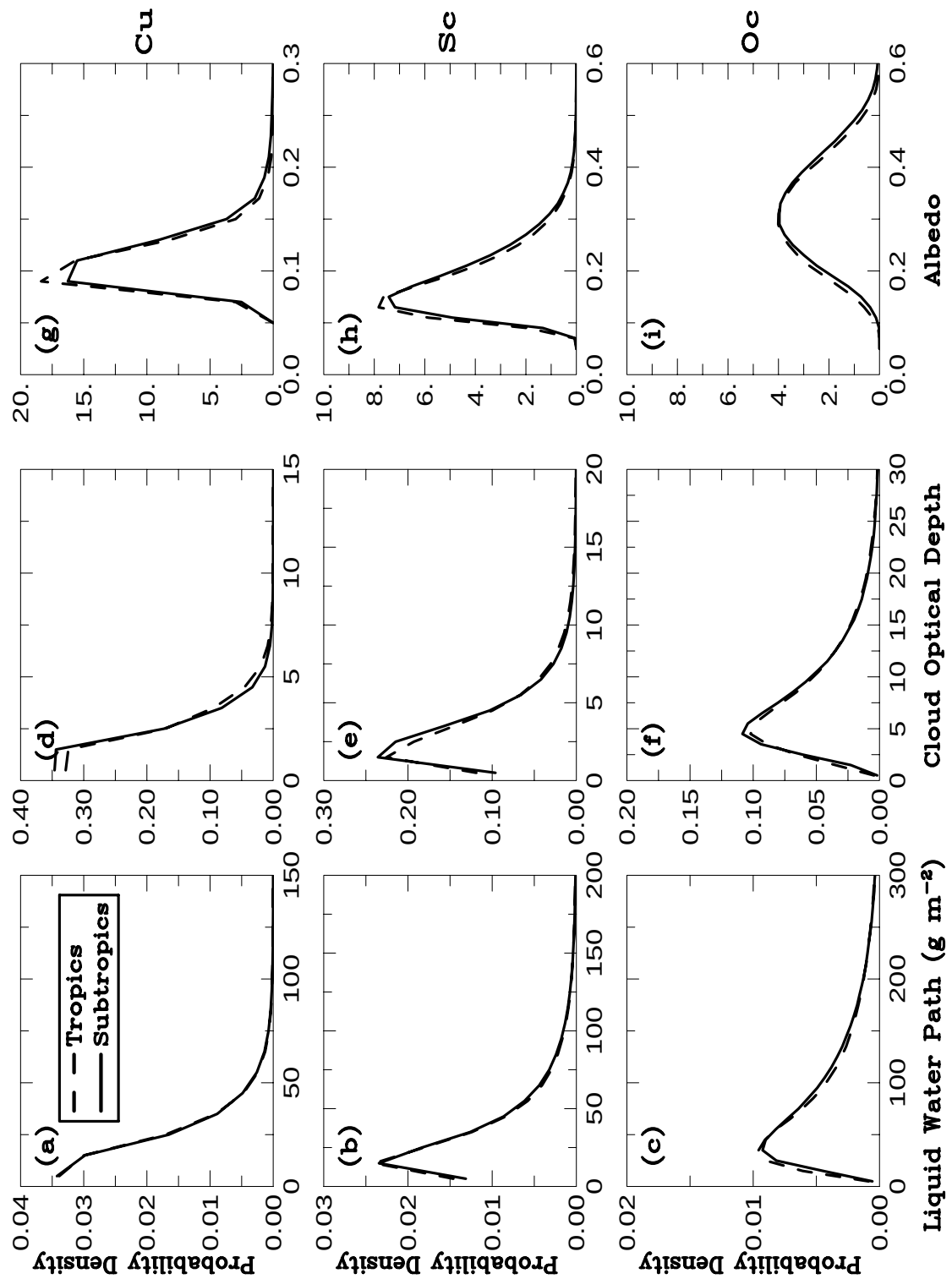

Figure 5. Summary histograms of liquid water path (a-c), cloud optical depth (d-f) and top-of-the-atmosphere albedo (g-i) for boundary-layer cumulus (a, d and g), stratocumulus (b, e and h) and overcast (c, f and i) cloud objects with equivalent diameters between 75 and 300 km in the tropical and subtropical regions for January - August 1998**.**

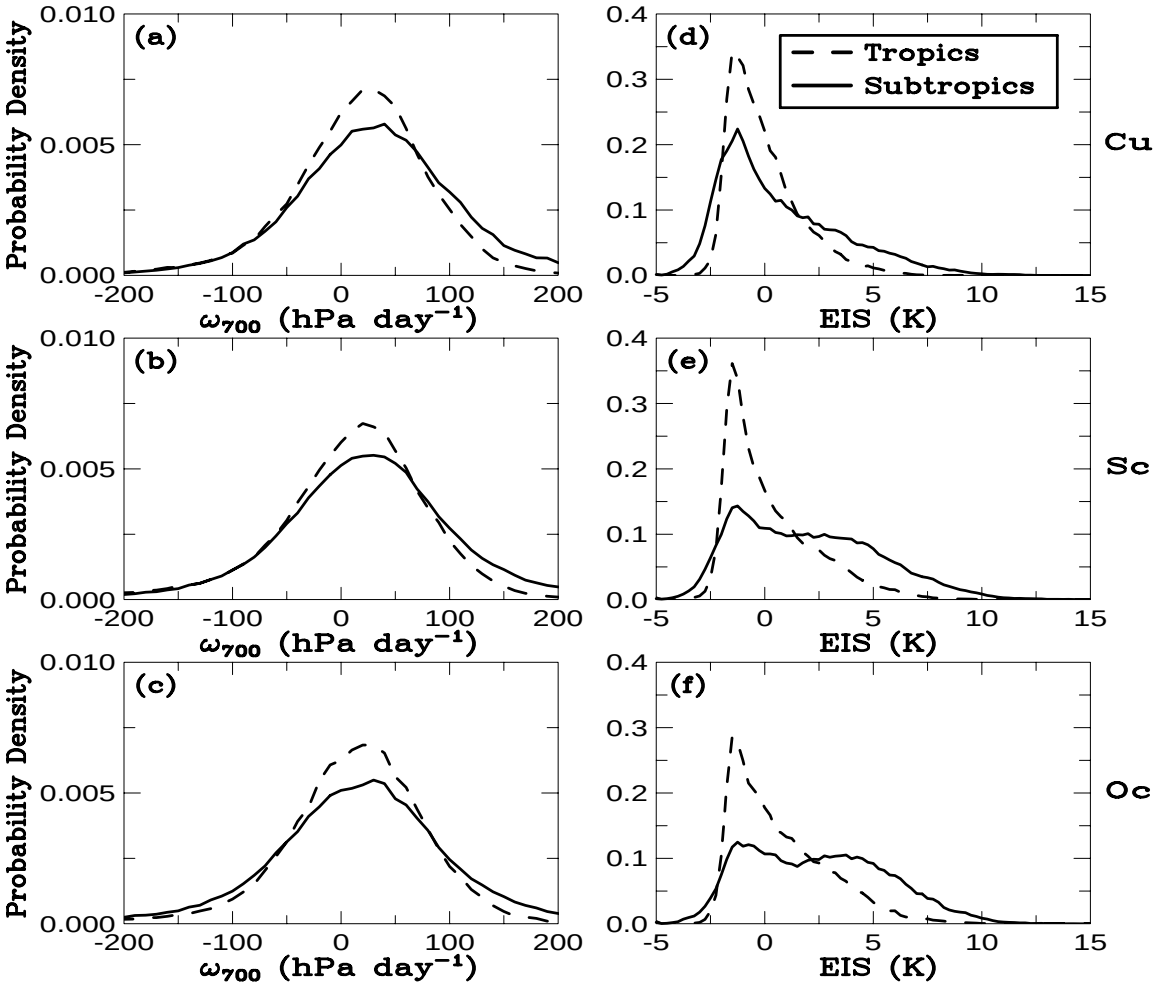

Figure 6. Histograms of cloud-object matched ω vertical velocity at 700 hPa (a-c) and estimate inversion strength (EIS; d-f) for cumulus (a, d), stratocumulus (b, e) and overcast (c, f) cloud object types in the tropics and subtropics. The EIS is defined in Wood and Bretherton (2006). S1, S2 and S3 size categories are included, as in Figs. 4 and 5. The numbers of ECMWF grid cells used in constructing these histograms are approximately 23%, 19% and 15% of the total footprint numbers listed in Table 4 for cumulus, stratocumulus and overcast types, respectively.

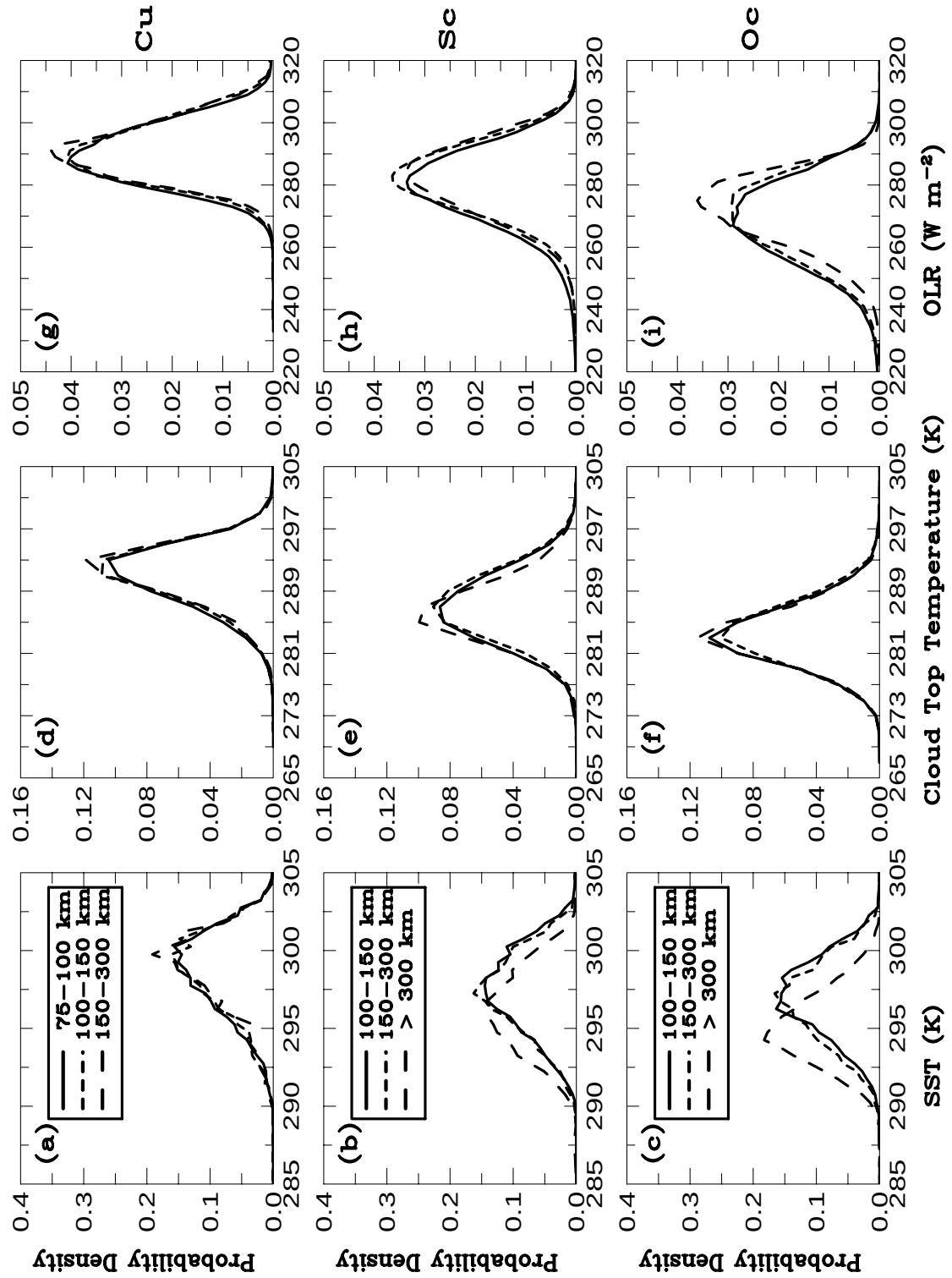

Figure 7. Same as Fig. 4 except for three size categories of subtropical cumulus (a, d and g), stratocumulus (b, e and h) and overcast (c, f and i) cloud objects. The cumulus size categories have equivalent diameters of 75-100 km, 100-150 km and 150-300 km, respectively. The stratocumulus and overcast size categories have equivalent diameters of 100-150 km, 150-300 km and greater than 300 km, respectively.

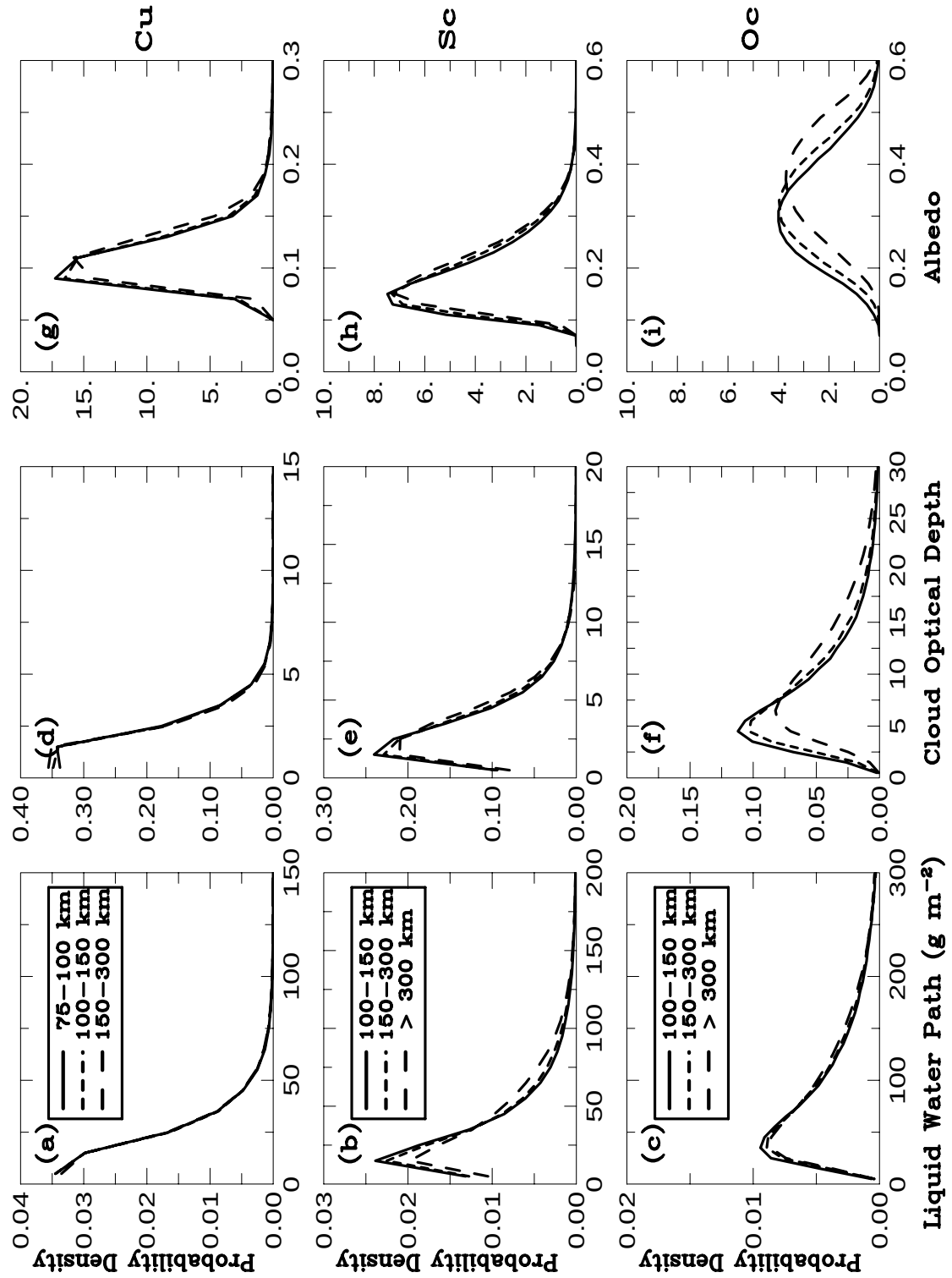

Figure 8. Same as Fig. 5 except for three size categories of subtropical cumulus (a, d and g), stratocumulus (b, e and h) and overcast (c, f and i) cloud objects. The cumulus size categories have equivalent diameters of 75-100 km, 100-150 km and 150-300 km, respectively. The stratocumulus and overcast size categories have equivalent diameters of 100-150 km, 150-300 km and greater than 300 km, respectively.

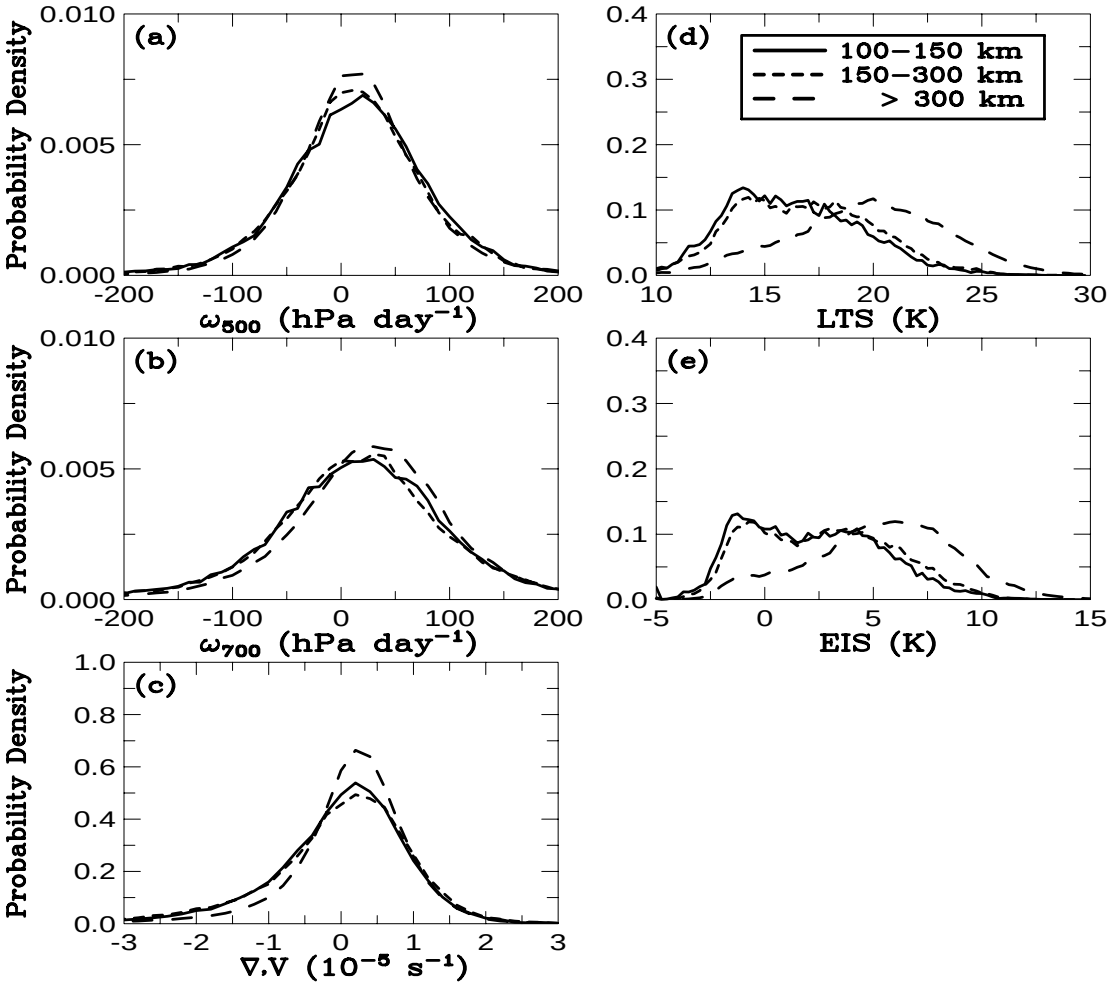

Figure 9. Histograms of cloud-object matched ω vertical velocity at 500 hPa (a) and 700 hPa (b), surface divergence (c), lower-tropospheric stability (d) and estimated inversion strength (EIS; e) for three size categories of the overcast cloud object type in the subtropical region. The lower-tropospheric stability is defined as the potential temperature difference between 700 and 1000 hPa by Klein and Hartmann (1993). The EIS is defined in Wood and Bretherton (2006).

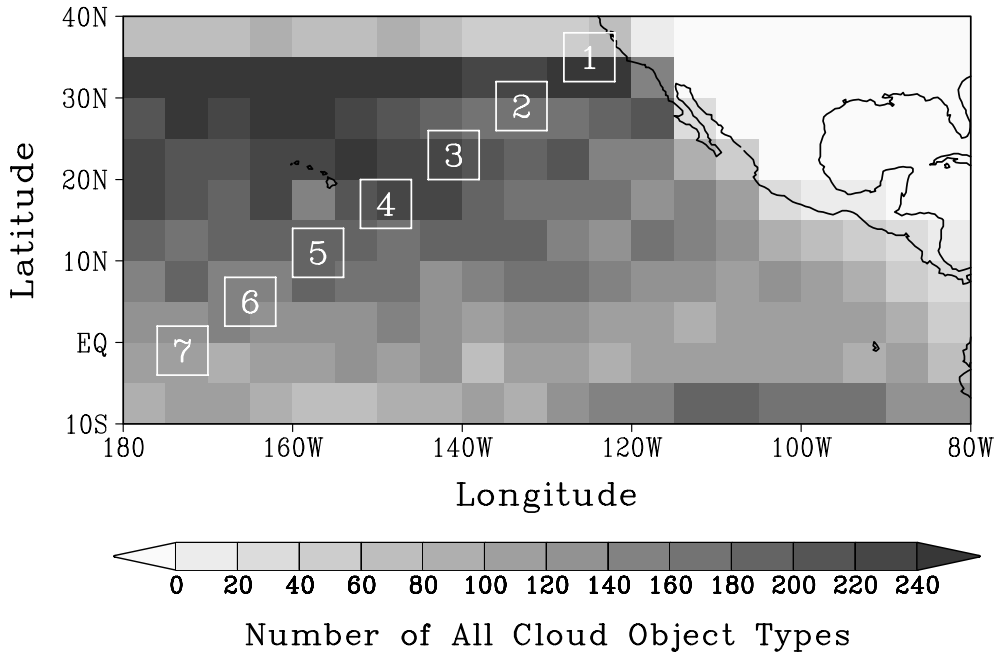

Figure 10. Locations of grids along a Pacific cross section (Grid 1-7) designed by the GCSS for a model intercompairson project. The accumulated number of all three cloud object types in 5° x 5° grids with equivalent diameters greater than 75 km is also shown.

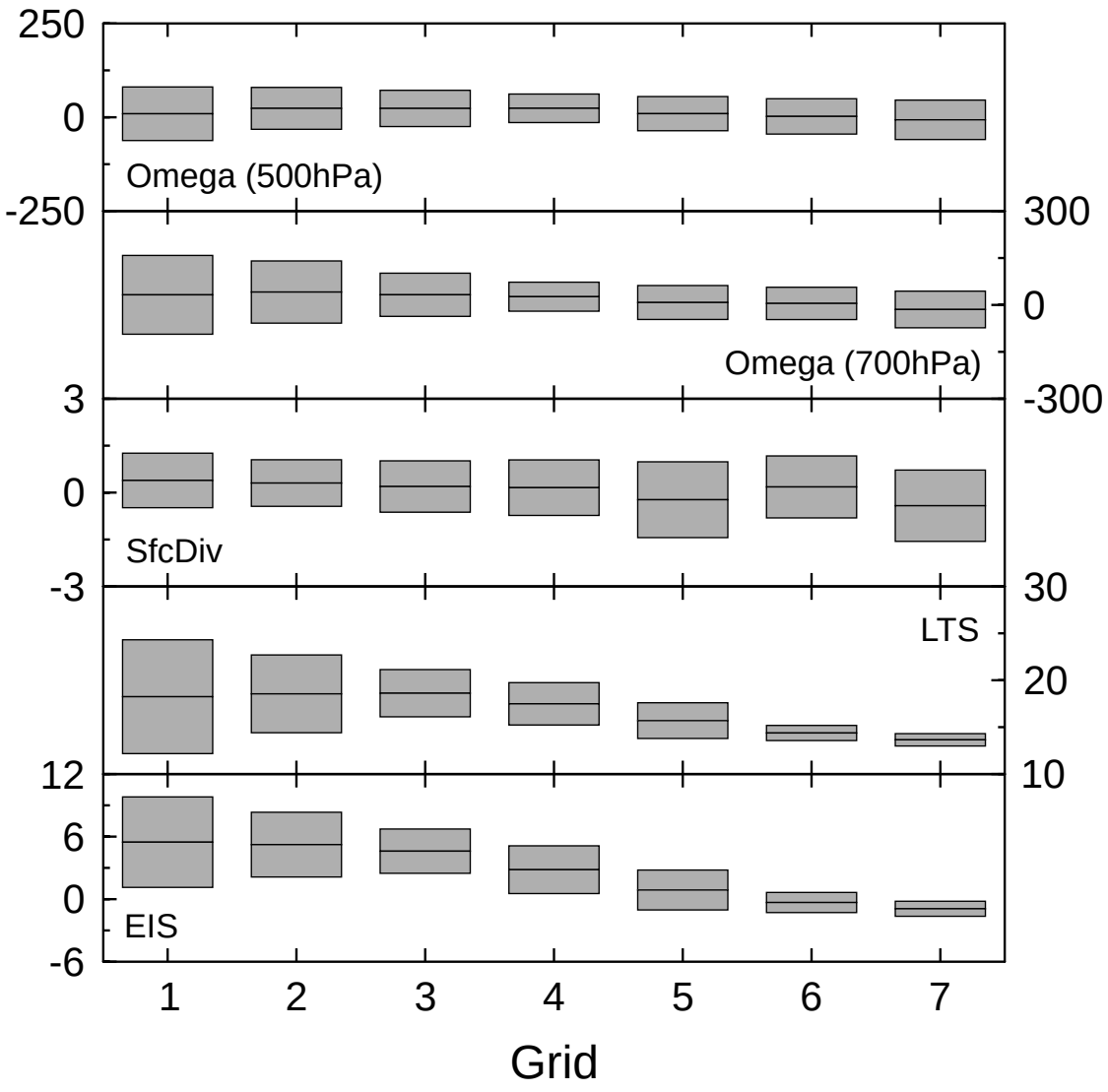

Figure 11. Eight-month (January - August 1998) means (lines within the bars) and standard deviations (vertical bars) of selected atmospheric-state parameters for Grids 1-7 of the GCSS Pacific transect: from the top to bottom panels, ω_{500}, ω_{700}, surface divergence, lower tropospheric stability [LTS; θ (700 hPa) - θ (1000 hPa)], and estimated inversion strength (EIS).

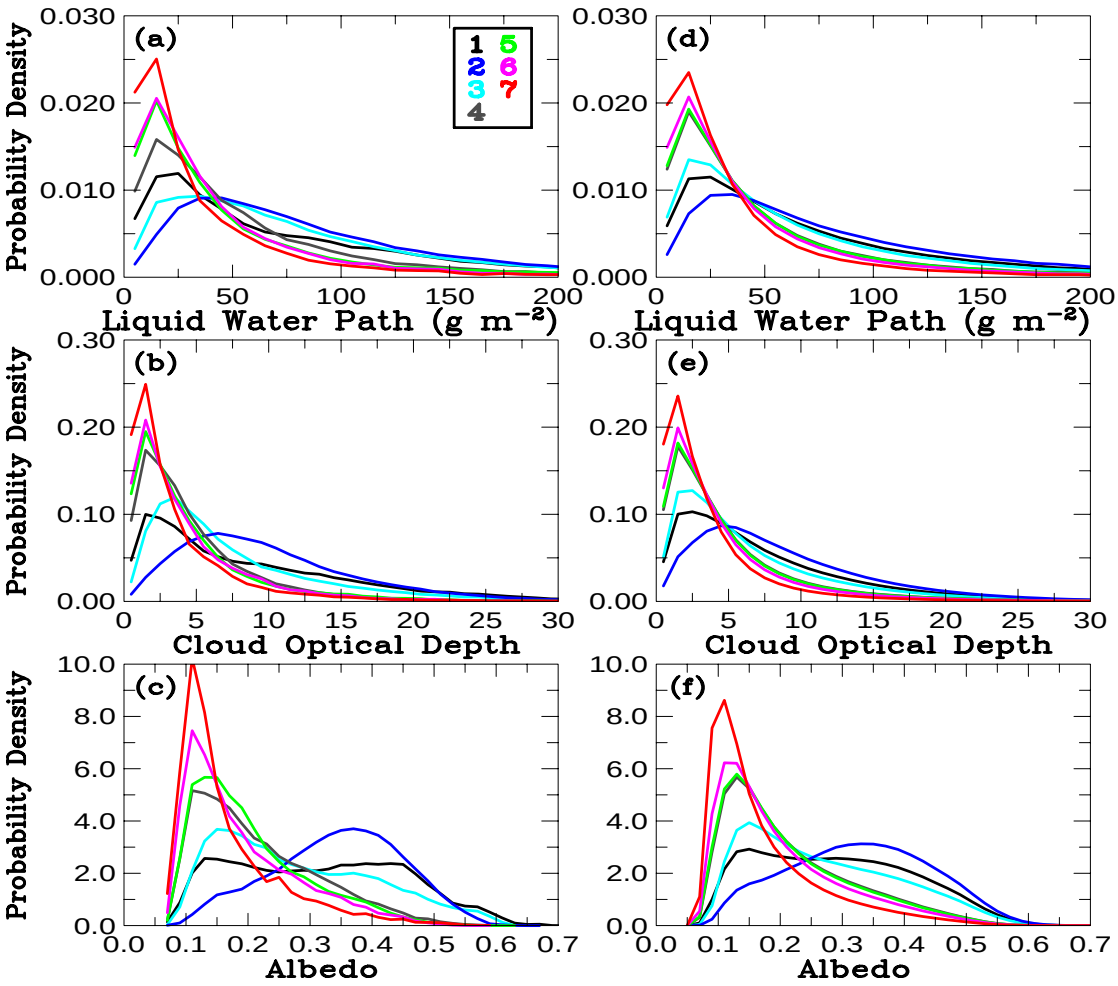

Figure 12. Summary histograms of liquid water path (a, d), cloud optical depth (b, e) and top-of-the-atmosphere albedo (c, f) for the combined cloud object types along the seven grids of the GCSS Pacific transect. Grid numbers along the transect are indicated by different colors. See Fig. 10 for the location of these grids. The left panels (a-c) are from observations while the right panels (d-f) are diagnosed from the observed proportions of cloud object types and histograms shown in Fig. 5.

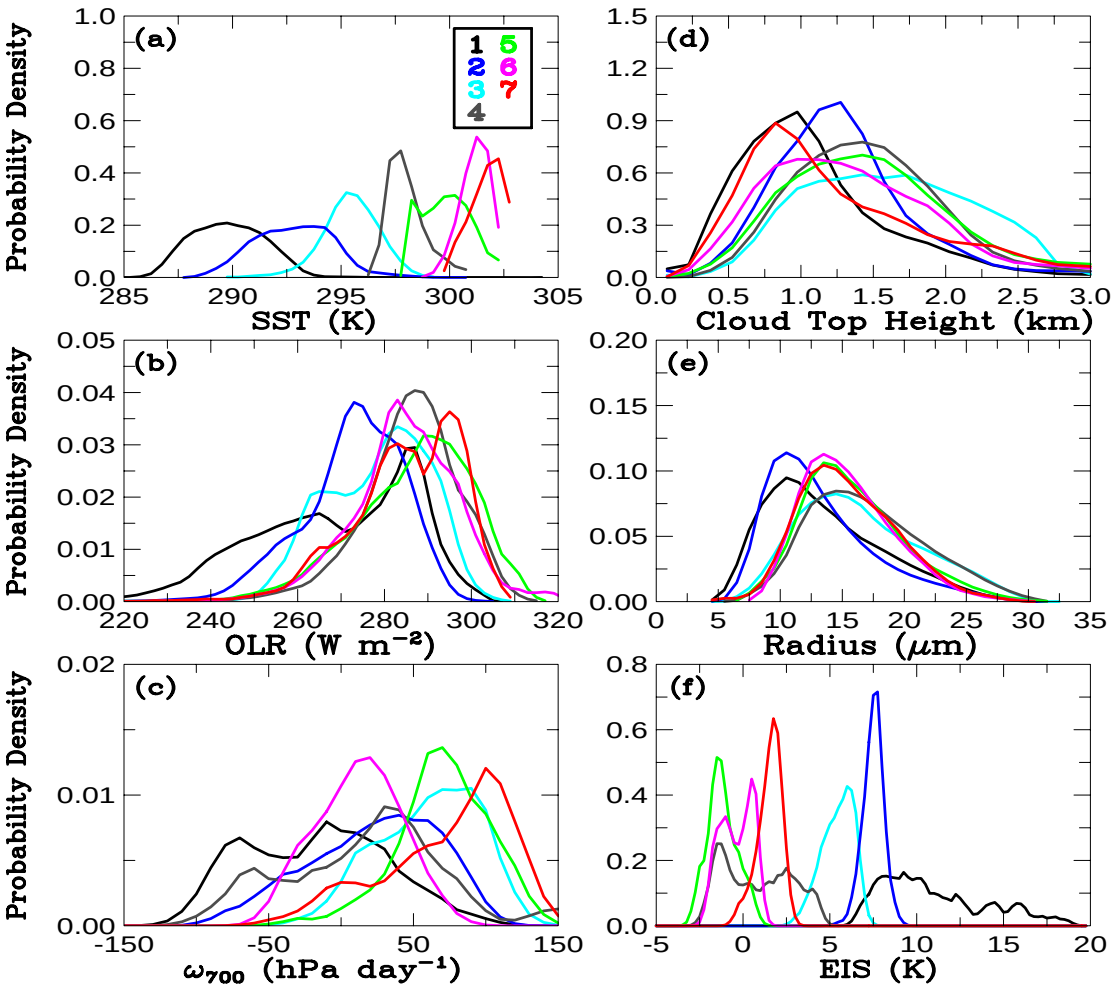

Figure 13. Same as Figs. 12a-c except for SST (a), OLR (b), ω_{700} (c), cloud-top height (d), droplet radius (e) and estimated inversion strength (f). A five-point (with weighting factors of 1/17, 3/17, 9/17, 3/17, 1/17) smoothing was applied to the histogram before plotting.

Table 1. A list of selection criteria for the boundary-layer cloud types.

Cloud object type	Cloud-top height	Cloud fraction	Latitude band
Cumulus	< 3 km	0.1 - 0.4	38 ° S - 38 ° N
Stratocumulus	< 3 km	0.4 - 0.99	38 ° S - 38 ° N
Overcast	< 3 km	0.99 - 1.0	38 ° S - 38 ° N

Table 2. The systematic biases and random errors in the measured footprint data of boundary-layer clouds and bin intervals of histogram used in this study.

Parameter	Systematic bias	Random error	Bin interval of histogram
OLR (W m^{-2})	< 0.5%	1-2%	4
TOA albedo	< 0.5%	2-3%	0.02
Cloud height (km)	0.2	0.3	0.15
Cloud temperature (K)	0.9	2.1	2.0
Liquid water path (g m^{-2})	-18	41	10.0
Droplet effective radius (μm)	0.7	1.8	1.0
Optical depth	-1.5	6.2	1.0

Table 3. Percent of the number of cloud-objects in the tropical and subtropical Pacific for four size categories of boundary-layer cumulus, stratocumulus and overcast cloud-object types during January-August 1998. The equivalent diameters of S1, S2, S3 and S4 size categories range from 75-100 km, 100-150 km, 150-300 km and > 300 km, respectively. The numbers of all-size (S1, S2, S3 and S4 combined) cloud objects of a given type are also shown in the table.

Cloud object type	Tropics					Subtropics				
	S1	S2	S3	S4	All sizes	S1	S2	S3	S4	All sizes
Cumulus	61.7	31.0	7.2	0.1	5,711	61.2	30.5	8.0	0.3	6,315
Stratocumulus	47.8	34.0	16.3	1.9	12,121	46.2	33.2	16.9	3.7	14,469
Overcast	40.5	32.6	21.3	5.6	4,025	38.0	30.5	20.2	11.3	6,139
All types	50.1	32.9	14.9	2.1	21,857	47.8	32.0	15.6	4.6	26,923

Table 4. Same as Table 3 except for the total footprint numbers, which are proportional to the total area coverages, for each size category in the tropical and subtropical regions. The total footprint numbers for all sizes are in thousands.

Cloud object type	Tropics					Subtropics				
	S1	S2	S3	S4	All sizes	S1	S2	S3	S4	All sizes
Cumulus	38.8	37.6	22.0	1.6	500.2	37.1	35.6	24.4	2.9	576.8
Stratocumulus	19.7	27.6	36.4	16.3	1640.4	15.4	21.7	30.6	32.3	2435.3
Overcast	11.0	17.5	34.4	37.1	830.3	5.5	8.8	17.3	68.4	2379.0
All types	20.5	26.4	33.4	19.7	2970.9	13.3	17.5	24.1	45.1	5391.1

Table 5. Statistics of the footprint numbers for the S4 size (equivalent diameters greater than 300 km) categories of boundary-layer cloud object types in the tropical and subtropical regions.

Cloud object type	Region	Mean	Median	Standard deviation	Minimum	Maximum
Stratocumulus	Tropics	1145	953	569	685	4579
	Subtropics	1459	1132	867	683	5679
Overcast	Tropics	1369	1035	1042	686	7384
	Subtropics	2350	1480	2132	684	15125

Table 6. The statistical significance levels or *p* values between a pair of size categories for different parameters of the three subtropical boundary-layer cloud object types. See text for the definition of size categories S1, S2, S3 and S4 and an explanation of *p* values.

Parameter	Cumulus			Stratocumulus			overcast		
	S1, S2	S2, S3	S1, S3	S2, S3	S3, S4	S2, S4	S2, S3	S3, S4	S2, S4
SST	0.49	0.78	0.39	0.44	< 0.01	< 0.01	0.13	< 0.01	< 0.01
OLR	0.22	0.74	0.08	< 0.01	0.06	< 0.01	0.14	< 0.01	< 0.01
Albedo	0.29	< 0.01	< 0.01	< 0.01	< 0.01	< 0.01	< 0.01	< 0.01	< 0.01
Cloud height	0.01	0.19	< 0.01	< 0.01	< 0.01	< 0.01	< 0.01	< 0.01	< 0.01
Cloud tempera-ture	0.04	0.31	0.01	< 0.01	< 0.01	< 0.01	0.09	0.04	0.55
LWP	0.97	0.65	0.70	< 0.01	< 0.01	< 0.01	0.01	0.17	< 0.01
Droplet radius	0.06	0.07	< 0.01	< 0.01	< 0.01	< 0.01	0.04	< 0.01	< 0.01
Optical depth	0.39	0.41	0.11	< 0.01	< 0.01	< 0.01	< 0.01	< 0.01	< 0.01

Table 7. Percent of total footprint number of each cloud object type observed in each 6° x 6° grid along the GCSS transect during January-August 1998. The total footprint number and cloud object number of all types are shown. See Fig. 10 for the location of each grid box.

Cloud object type	Grid 1	Grid 2	Grid 3	Grid 4	Grid 5	Grid 6	Grid 7
Cumulus	3.8	0.3	1.3	9.3	10.4	17.5	36.6
Stratocumulus	34.8	17.5	50.6	62.2	62.6	60.7	50.4
Overcast	61.4	82.2	48.1	28.5	27.0	21.8	13.0
All types--total footprint	97718	175762	76837	38499	29615	20408	11707
All types--number	197	163	172	166	149	97	67